J. Mech. Phys. Solids 205 (2025) 106339

Contents lists available at ScienceDirect

Journal of the Mechanics and Physics of Solids

journal homepage: www.elsevier.com/locate/jmps

Biaxial characterization of soft elastomers: Experiments and data-adaptive configurational forces for fracture

Miguel Angel Moreno-Mateos [a,*,1], Simon Wiesheier [a,1], Ali Esmaeili [b], Mokarram Hossain [b], Paul Steinmann [a,c]

[a] Institute of Applied Mechanics, Friedrich-Alexander-Universität Erlangen–Nürnberg, Egerlandstr. 5, 91058, Erlangen, Germany
[b] Zienkiewicz Institute for Modelling, Data and AI, Faculty of Science and Engineering, Swansea University, SA1 8EN, Swansea, United Kingdom
[c] Glasgow Computational Engineering Centre, School of Engineering, University of Glasgow, G12 8QQ, United Kingdom

ARTICLE INFO

Dataset link: https://doi.org/10.5281/zenodo.15187640

Keywords:
Finite strains
Data-driven constitutive modeling
Parameter identification
Material model discovery
Soft fracture
Configurational Force Method

ABSTRACT

Understanding the fracture mechanics of soft solids remains a fundamental challenge due to their complex, nonlinear responses under large deformations. While multiaxial loading is key to probing their mechanical behavior, the role of such loading in fracture processes is still poorly understood. Here, we present a combined experimental–computational framework to investigate fracture in soft elastomers under equi-biaxial loading. We report original equi-biaxial quasi-static experiments on five elastomeric materials, revealing a spectrum of material and fracture behavior — from brittle-like to highly deformable response with crack tip strains exceeding 150 %. Motivated by these observations, we develop a hybrid computational testbed that mirrors the experimental setup and enables virtual biaxial tests. Central to this framework are two components: a data-adaptive formulation of hyperelastic energy functions that flexibly captures material behavior, and a post-processing implementation of the Configurational Force Method, providing a computationally efficient estimate of the J-integral at the crack tip. Our data-adaptive framework for hyperelastic energy functions proves versatility to capture with high accuracy the hyperelastic behavior observed in the biaxial experiments. This is important because accurately capturing the constitutive behaviour of soft solids is key for a reliable application of the Configurational Force Method to soft solids. In the limit of crack onset, a critical value of the crack tip configurational force allows for a criterion of fracture toughness. Together, our experimental, theoretical, and computational contributions offer a new paradigm for characterizing and designing soft materials with tailored fracture properties.

1. Introduction

Soft materials such as elastomers and hydrogels exhibit complex material response at large deformations. These properties pose significant challenges for constitutive modeling, particularly under multiaxial loading conditions. Comprehensive characterization of these behaviors is critical, given the widespread use of soft materials in biomedical devices, soft robotics, and flexible electronics (Zhao, 2017; Moreno-Mateos et al., 2022; Arif et al., 2024). Despite their relevance, experimental studies under biaxial loading remain relatively limited. Seminal contributions include the early work by Treloar (1944) and later investigations by James et al. (1975), Kawabata et al. (1981), and more recent the study by Pancheri and Dorfmann (Pancheri and Dorfmann, 2014).

* Corresponding author.
E-mail address: miguel.moreno@fau.de (M.A. Moreno-Mateos).
[1] MA Moreno-Mateos and S Wiesheier contributed equally to this work.

https://doi.org/10.1016/j.jmps.2025.106339
Received 26 May 2025; Received in revised form 30 July 2025; Accepted 25 August 2025
Available online 2 September 2025
0022-5096/© 2025 The Authors. Published by Elsevier Ltd. This is an open access article under the CC BY-NC license (http://creativecommons.org/licenses/by-nc/4.0/).

List of Symbols & Abbreviations

$\hat{\bullet}$	Volumetric part of $\bullet$
$\bar{\bullet}$	Isochoric part of $\bullet$
$\mathscr{B}_0$	Material configuration
$\mathbf{C}$	Right Cauchy Green deformation tensor
$\mathbf{F}$	Deformation gradient
$\mathbf{F}_{\text{CNF}}$	Nodal configurational forces
J	Determinant of deformation gradient
$\bar{I}_1$	First isochoric invariant
$\bar{I}_2$	Second isochoric invariant
$\mathbf{I}$	Second order unit tensor
$\mathcal{L}$	Objective function
$\mathbf{P}$	Piola stress tensor
Ψ	Strain energy density
$\Psi^{(\mathcal{I},\mathcal{D})}$	Interpolation-based strain energy density on interpolation domain $\mathcal{D}$
p	Hydrostatic pressure
R	Finite element residual vector
$\boldsymbol{\Sigma}$	Eshelby energy–momentum tensor
θ	Vector of parameters for optimization
$\mathbf{u}$	Displacement
$\mathbf{X}$	Material coordinates
$\mathbf{x}$	Spatial coordinates
DIC	Digital Image Correlation
FEM	Finite Element Method
FEMU	Finite Element Model Updating
NN	Neural Network
PINN	Phyics Informed Neural Network
ROI	Region of Interest

These efforts provide valuable insights into the complex mechanical response of soft materials under biaxial stretching. However, comprehensive experimental datasets are limited and studies extending beyond basic material characterization — such as those investigating the fracture behavior of soft materials — remain exceptionally rare (Ahmad et al., 2019; Khiêm et al., 2019; Esmaeili et al., 2023).

1.1. Fracture & configurational mechanics

Classical fracture mechanics approaches include the energy release rate (Griffith, 1921), stress intensity factors (Irwin, 1957), the J-integral (Cherepanov, 1967; Rice, 1968; Shih et al., 1986), and the crack tip opening displacement (Wells, 1961). For mixed-mode crack propagation, various deflection criteria have been proposed, such as the maximum tangential stress criterion (Erdogan and Sih, 1963), the strain energy density S-factor (Sih, 1974), the maximum energy release rate criterion (Hussain et al., 1974), and the apparent crack extension force approach (Strifors, 1974). These established methods are primarily grounded in Linear Elastic Fracture Mechanics (LEFM). At finite strains, the crack tip often exhibits pronounced blunting (Hui et al., 2003; Qi et al., 2019; Lu et al., 2021), rendering many LEFM assumptions inapplicable. Only a limited number of closed-form solutions exist that analytically describe the deformed crack contour and the near-tip fields in soft materials (Long et al., 2011; Long and Hui, 2015).

Configurational mechanics offers a theoretical framework to quantify the driving forces that produce changes in the material configuration due to the evolution of defects (Eshelby, 1951; Steinmann, 2000; Podio-Guidugli, 2002; Gross et al., 2003; Steinmann, 2008; Steinmann et al., 2009; Steinmann, 2022). These changes are consistent with a principle of maximal energy dissipation. The energy released during such configurational changes can be described in terms of configurational forces, which are power or variationally conjugated to variations in the material configuration. As such, configurational forces act on the material manifold and drive changes in the material positions.

Computational fracture mechanics offers a range of modeling strategies, many of which are rooted in the energy-based variational approach introduced by Francfort and Marigo (1998). Among others, we mention: non-local damage models with internal history variables and non-local strain measures (Schreyer, 1990; Peerlings et al., 1998; Jirásek, 1998); element deletion method (Song et al., 2008); cohesive zone models with traction-separation laws (Dugdale, 1960); extended finite element method (XFEM) (Moës et al., 1999); mesh-free methods (Belytschko et al., 1995); phase-field methods model fracture (Miehe et al., 2010; Kumar et al., 2020; Lo et al., 2022; Moreno-Mateos et al., 2023; Moreno-Mateos and Steinmann, 2024b; Dammaßet al., 2024b; Hu and Li, 2025); eigenfracture (Schmidt et al., 2009; Storm and Kaliske, 2023); peridynamics (Silling, 2000; Javili et al., 2021).

Configurational forces[2] find their most widespread application in the field of fracture mechanics. The contour integral form of the celebrated J-integral (cf., e.g., Shih et al., 1986) is mathematically equivalent to the configurational force at the crack tip. *Pacman-shaped* domains enclosing the crack tip have been used to prove this equivalency (Moreno-Mateos and Steinmann, 2024a). The Configurational Force Method identifies the crack tip configurational force — computed as nodal forces resulting from a finite element discretization of the Eshelby stress tensor — as a direct and effective estimator of the J-integral (Steinmann et al., 2001). While both the Equivalent Domain Integral method — transformation of the contour J-integral into an area or volume domain integral (Li et al., 1985; Moran and Shih, 1987; Shivakumar and Raju, 1992) — and the Configurational Force Method are theoretically equivalent, the latter offers notable computational advantages within a finite element framework. Discrete Eshelby-like forces are derived using the same interpolation scheme applied in the Galerkin discretization of the weak form. After defining the Eshelby stress tensor in its energy–momentum form, this interpolation procedure can be efficiently implemented within a postprocessing code. In contrast, the domain integral method requires constructing an ad hoc weight function — typically linearly varying from the value one at the crack tip to the value zero at the outer boundary of the evaluation domain — to compute the J-integral as a domain integral. Moreover, whereas the domain integral method must be coupled with the virtual crack extension method (Budiansky and Rice, 1973; Hussain et al., 1974) to determine crack propagation in assumed directions, the Configurational Force Method inherently provides both the magnitude and direction of the driving forces, making it particularly well suited for adaptive fracture simulations. In this context, several authors have proposed crack propagation laws grounded in configurational mechanics (Steinmann et al., 2001; Kienzler et al., 2002; Denzer et al., 2003; Gurtin and Podio-Guidugli, 1996; Zhou et al., 2022), including derivations for curved crack paths (Schütte, 2009; Frankl et al., 2022; Schmitz and Ricoeur, 2023) and strain gradient elasticity formulations (Serrao and Kozinov, 2025b). Other contributions include configurational criteria for mixed-mode fracture (Guo and Li, 2017) and extensions to fatigue failure (Liu et al., 2020; Yan et al., 2023). Inelastic fracture behavior has been explored in the context of plasticity and creep (Nguyen et al., 2005; Näser et al., 2007; Kaliske et al., 2009; Özenç et al., 2014; Kolednik et al., 2022). Coupled-field problems have also benefited from this approach, including electro-viscoelastic fracture (Denzer and Menzel, 2014), fracture of dielectric electro-active elastomers (Moreno-Mateos et al., 2024), and flexoelectric materials (Serrao and Kozinov, 2025a). A recent development is configurational peridynamics (Steinmann et al., 2023). These examples illustrate the breadth of applications where configurational mechanics provides a powerful and unified perspective on fracture phenomena.

Interestingly, the advancement in configurational mechanics has shown that configurational forces can serve as a standalone and sufficient framework to describe fracture mechanics of soft materials at finite strains (Moreno-Mateos and Steinmann, 2024a). Calculating the configuration forces at the tip of the crack must yield a value equal to the J-integral, eliminating the need for analytical solutions. The results may be as accurate as the constitutive model utilized to solve the boundary value problem.

1.2. Data-adaptive constitutive modeling

Accurate constitutive modeling, essential for capturing material behavior, is necessary to compute reliable configurational forces. Traditionally, material model calibration is based on phenomenological models whose parameters are fitted to experimental data. A wide variety of phenomenological models exist; we refer to Steinmann et al. (2012), Ricker and Wriggers (2023) for state-of-the-art reviews. In recent years, data-driven constitutive modeling approaches have gained increasing attention, as they alleviate the need to predefine a specific model form and move toward model-free or model-discovery paradigms (Dal et al., 2023; Tikenoğullarıet al., 2023). Notable among these is the work by Kirchdoerfer and Ortiz (2016), where each quadrature point is assigned the nearest state from the data set. As the field has matured, multiple research streams have emerged. These range from symbolic regression (Abdusalamov et al., 2023; Bahmani and Sun, 2024) and Gaussian Process Regression (Frankel et al., 2019; Ellmer et al., 2024) to various neural network (NN)-based approaches (Holthusen et al., 2024).

Several NN formulations have recently been proposed. Physically-Informed Neural Networks (PINNs) (Hamel et al., 2023) are a promising tool for solving inverse problems. They aim to replace the calibration process with a neural network that simultaneously identifies material and network parameters, but they typically assume the underlying material model is known. In contrast, physics-augmented (PANN) (Dammaßet al., 2024a; Klein et al., 2025; Ortigosa et al., 2025) and constitutive artificial neural networks (CANN) (Linka, 2021; Linka and Kuhl, 2023; Linden, 2023) are designed to discover new constitutive models directly from data. In all such approaches, the physical knowledge is incorporated by adapting the network architecture to identify plausible and physically consistent models. We refer to Fuhg (2025), Römer et al. (2024) for comprehensive reviews on data-driven constitutive laws and calibration techniques.

Experimental data for model calibration are often obtained from simple load cases such as uniaxial or simple shear, which typically result in homogeneous deformation fields. While such experiments are easy to conduct, the resulting data often lack the richness needed to calibrate versatile material models. An alternative is to use more complex geometries and loading conditions that produce inhomogeneous deformation fields. Digital Image Correlation (DIC) (Sutton et al., 2009) enables the extraction of full-field displacement measurements from these experiments. Together with global force data, this provides a rich experimental dataset for calibration. Common parameter identification approaches are Finite Element Model Updating (FEMU) and the Virtual Fields Method (VFM) (Pierron and Grédiac, 2012). FEMU involves iteratively solving the boundary value problem using the Finite Element Method to replicate the experimental setup. Its main strength lies in the ability to leverage well-established FEM and optimization algorithms. The Efficient Unsupervised Constitutive Law Identification and Discovery (EUCLID) framework works

[2] Configurational forces are also referred to as material forces.

similarly to the VFM where displacement fields are leveraged to construct the stress field. EUCLID works by prescribing a set of canonical material models and filtering the dominant material models using sparse regression, leaving a constitutive law described by only a sparse set of the prescribed material models (Flaschel, 2023). Extensions of the original approach, including Bayesian interference (Bayesian-EUCLID) (Joshi, 2022) and neural networks (NN-EUCLID) (Thakolkaran et al., 2022) have already been developed.

1.3. Our approach: data-adaptive configurational forces

Despite the body of work in the experimental mechanics of soft solids, data-driven model discovery, and theoretical and computational fracture mechanics, several important gaps in knowledge remain, to the best of the authors' knowledge. These are: (i) experimental data on constitutive behavior of soft materials under biaxial conditions are limited; (ii) experimental data on fracture behavior of soft materials in biaxial loading settings are similarly scarce, if not inexistent; (iii) data-driven modeling approaches have been only marginally applied to biaxial experimental data; (iv) the Configurational Force Method—as an estimator of the J-integral—has not yet been employed in combination with data-adaptive constitutive models, nor has it been applied to soft elastomers under biaxial loading conditions. Furthermore, the intersection of these four points is *terra incognita*.

Here, we present a comprehensive study that integrates experiments with a novel computational framework for data-adaptive configurational forces in fracture mechanics. On the one hand, we report a comprehensive experimental characterization of soft elastomers under equi-biaxial, quasi-static[3] loading conditions. We provide the results in the main manuscript and also the complete dataset in a Zenodo repository. The experimental insights into the (a) constitutive and (b) fracture behavior span from brittle constitutive/fracture responses to remarkably soft ones, i.e., highly non-linear at strains above $150\,\%$ at the crack tip, depending on the material. The experimental observations are then utilized to motivate a hybrid computational framework able to inform and further expound the experiments—in terms of constitutive behavior *ante* fracture onset and fracture toughness. The framework is built upon two core components: (i) a data-adaptive formulation of hyperelastic energy functions, and (ii) the Configurational Force Method implemented as a post-processing algorithm.

We propose a versatile, data-adaptive framework for calibrating hyperelastic energy functions by combining FEMU with a novel data-adaptive constitutive modeling approach. In our framework, constructed in the sequel of a previous work of the authors in Wiesheier et al. (2024), the strain energy function is represented via B-spline interpolation defined over the space of invariants. Unlike phenomenological models, this approach makes no assumptions about the shape of the energy function. Instead, its form is determined by a set of interpolation points (defined in the invariant space) and the corresponding values, both identified automatically using robust non-linear optimization. In the present work, the framework utilizes original experimental data on five different soft elastomers under equi-biaxial conditions consisting of global reaction forces and full-field displacements obtained through DIC. In turn, the Configurational Force Method is implemented as postprocessing algorithm that calculates the Eshelby stress tensor and its corresponding nodal forces, i.e., configurational forces. The total configurational force at the crack tip estimates the J-integral. This approach offers a simpler alternative compared to traditional methods that rely on evaluating a contour integral around the crack tip. In the sequel of a previous work of the authors (Moreno-Mateos and Steinmann, 2024a), here the Configurational Force Method enables fracture assessment in soft materials under biaxial loading conditions. Overall, by integrating rich biaxial data sets with a flexible, data-adaptive constitutive model, our approach offers a powerful tool to accurately capture complex material behavior. This is paramount because accurately capturing the constitutive behavior of soft elastomers is key for a reliable application of the Configurational Force Method to soft solids.

2. Experimental characterization of soft elastomers under biaxial loading

A comprehensive experimental characterization of soft elastomers offers novel insights into the constitutive behavior (*ante* fracture onset) and the fracture behavior under equi-biaxial conditions. Furthermore, the material characterization is central in this work as it will allow for accurate constitutive models and determination of configurational forces for fracture assessment.

The results are detailed in the main manuscript and the dataset is available in the following Zenodo repository:

- https://doi.org/10.5281/zenodo.15187640.

2.1. Materials, synthesis, and experimental setup

We prepared five soft elastomers with stiffnesses ranging from $5\,\mathrm{kPa}$ to $350\,\mathrm{kPa}$. Four of them were synthesized by curing two-component blends at elevated temperatures: Elastosil P7670 for three different volume mixing ratios, and Sylgard 184. The fifth material is VHB Tape, which is supplied by the manufacturer as pre-formed sheets that can be cut to size. Additional details about the materials are provided below.

[3] Only the quasi-static behavior of the materials at very low stretch rates is considered in this work.

- Elastosil P7670 2:1 (softest), 8:5 (medium), and 1:1 (stiffest) (Wacker Chemie AG, Munich, Bavaria, Germany) was synthesized mixing two raw phases (phase A and B) to form a crosslinked silicone elastomer. The mixing ratio of the phases is defined as the volume ratio between the phases V_A/V_B, with V_A and V_B the volume of the phase A and B, respectively. The three polymer variants are 2:1, 8:5, and 1:1, respectively from the softest to the stiffest (cf. the previous work of the authors (Moreno-Mateos and Steinmann, 2024b) for additional variants of the elastomer). Each mixture was cast into an open polytetrafluoroethylene (PTFE) mold, degassed under vacuum for 15 min, and cured in an oven at 120 °C for 2 h. The resulting square samples had a uniform thickness of $t = 2$ mm.
- Sylgard 184 (Dow Inc., Midland, Michigan, United States) was prepared mixing two raw phases in a 10:1 volume ratio, resulting in a crosslinked material stiffer than all Elastosil P7670 variants. As with the Elastosil samples, the mixture was cast into an open mold, degassed under vacuum for 15 min, and cured in an oven at 120 °C. The final cured sample also had a thickness of $t = 2$ mm.
- VHB 4905 Tape (3M, Saint Paul, Minnesota, United States) was supplied by the manufacturer as pre-formed sheets of thickness $t = 0.5$ mm, which were cut to the desired dimensions. Among all tested elastomers, VHB exhibited the most pronounced viscoelastic behavior. To minimize rate-dependent inelastic effects, all tests involving VHB were conducted at low strain rates ($0.01\,s^{-1}$).

The experimental testbed consisted of a bespoke biaxial testing machine and an imaging system. The biaxial machine (eXpert 8000, ADMET, Norwood, MA, United States) is equipped with a lateral sliding pinching grip system allowing the gripping fingers positioned at the corners to translate perpendicular to the loading direction, i.e., in the direction of the edge of the sample, as the material expanded (see Fig. 1.a). The initial distance between clamps was $l_0 = 85$ mm for all tests. Equi-biaxial experiments were carried out up to complete rupture on samples featuring an initial notch of 10 mm centered and oriented at 45° with respect to the loading axes of the testing machine (see Fig. 1.a). A quasi-static stretch rate of $0.01\,s^{-1}$, i.e., displacement rate of the axes of $0.85\,mm\,s^{-1}$ divided by the initial distance between clamps of 85 mm, was used for all tests. Note that Sylgard and Elastosil — all its variants — show moderate rate-dependent behavior while VHB is the most inelastic one. To minimize the influence of rate-dependent effects in VHB, a low quasi-static stretch rate was selected for the experimental campaign.

The biaxial machine was equipped with a 5.0-megapixel CCD digital camera (2448 × 2028 @ 75 fps) and a 2D DIC System analysis software (VIC-2D, Correlated Solutions, Inc.). DIC was used to compute the displacement fields, which served as input for calibrating data-adaptive hyperelastic strain energy functions — an essential step for accurately computing fracture configurational forces, as detailed in subsequent sections. The camera was mounted perpendicular to the surface of the sample, providing a fixed length-to-pixel scale of 0.028 930 9 mm/pixel. A hybrid method was employed to apply the speckle pattern. First, the sample surfaces were uniformly sprayed with black paint. Then, a pad featuring a predefined surface pattern was used to imprint a structured speckle pattern on top of the sprayed layer. For postprocessing the displacement fields, a subset of 29 pixel and a step size of 7 pixel were used.[4] In addition, engineering strain fields were derived from the displacement data by computing the Lagrange strain tensor, $\mathbf{E} = \frac{1}{2}[\mathbf{C} - \mathbf{I}]$, with $\mathbf{C}$ the right Cauchy–Green tensor and $\mathbf{I}$ the second order identity tensor, making the results insensitive to arbitrary rigid-body motion. Note that the strain fields will not be necessary to calibrate the data-adaptive strain energy functions, which work only on displacement fields. However, we present the strain fields as they provide valuable insight for interpreting the constitutive behavior near the crack tip and for comparing the mechanical response of the different materials.

2.2. Results

The experimental characterization highlights a range of fracture behaviors, from brittle-like failure in Sylgard to highly nonlinear fracture responses in VHB Tape. The corresponding force–displacement results are shown in Fig. A.13 for all experimental repetitions. Here, to facilitate the discussion and provide a more intuitive basis for interpreting the material response, Fig. 2 displays average engineering stress–strain curves.

Key metrics derived from the experiments include the total work of fracture and the average strain at failure. Fig. 3 presents bar plots of the total work of fracture per unit volume[5] for all tested materials, except Elastosil 1:1.[6] Among all materials, VHB Tape exhibits the highest fracture energy at $0.1624\,mJ\,mm^{-3}$, which is 1376 % higher than Sylgard, 1709 % higher than Elastosil 2:1, and 335 % higher than Elastosil 8:5. In contrast, Sylgard, Elastosil 2:1, and Elastosil 8:5 exhibit fracture energy values of $0.0118\,mJ\,mm^{-3}$, $0.0095\,mJ\,mm^{-3}$, and $0.0485\,mJ\,mm^{-3}$, respectively. Notably, despite being synthesized from the same base components, Elastosil 8:5 shows a markedly higher work of fracture than Elastosil 2:1 — a difference of 511 % — highlighting the strong influence of mixing ratio on fracture behavior. The average strain at failure—computed by dividing the clamp displacement by the initial grip separation (l_0)[7] — follows a trend consistent with the work of fracture. VHB again shows the highest value (104 %), while Sylgard fails at the lowest strain (5.9 %). Elastosil 2:1 and 8:5 fall in between, with average failure strains of 46.9 % and 61.8 %, respectively. However, in this case, the increase for Elastosil 8:5 relative to Elastosil 2:1 is more modest — only 132 %. This suggests that while the increased crosslink density in Elastosil 8:5 significantly raises the energy dissipation capacity, it does not proportionally extend the stretchability before rupture.

[4] For accurate DIC measurements, the subset size is typically recommended to be at least three times larger than the step size.

[5] In the literature, the total work of fracture is often decomposed into essential and non-essential components. The essential part corresponds to the energy dissipated in the immediate vicinity of the crack tip, i.e., the fracture process zone — and is considered an intrinsic material property. The non-essential part accounts for energy dissipated in the surrounding bulk material. This study does not attempt to distinguish between these two contributions.

[6] Elastosil 1:1 did not reach complete rupture due to its tendency to fracture laterally. Instead, samples slipped out of the clamps, a behavior attributed to the extreme stretchability enabled by sideways fracture paths (see Moreno-Mateos and Steinmann, 2024b).

[7] The average strain at failure provides an average, global measure that does not capture the local strain concentration near the crack tip but that aims at describing the homogeneous structural strain in the direction of the axes.

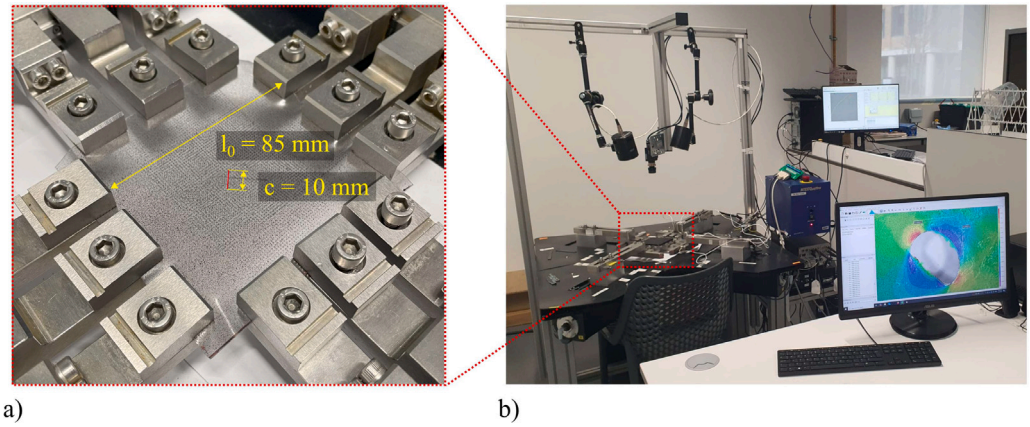

Fig. 1. Experimental setup for biaxial stretch tests. (a) Close-up view of the grips used in the experimental testbed. Each grip consists of three independent clamps designed to hold rectangular specimens. A sliding grip system allows the gripping fingers to translate perpendicular to the loading direction, i.e., in the direction of the edge of the sample. To that end, the gripping fingers can freely move in this direction. Insets: the initial configuration shows the separation between opposing grips and a centrally positioned notch in the specimen, inclined at an angle of 45° relative to the loading axis. This orientation ensures symmetric deformation with respect to the axis of the pre-cut. (b) Overview of the experimental setup, featuring the DIC imaging system mounted above the specimen. The testbed includes two orthogonal pairs of grips that enable biaxial tensile loading. The setup is connected to control and acquisition computers used to operate the system and record images throughout the deformation process.

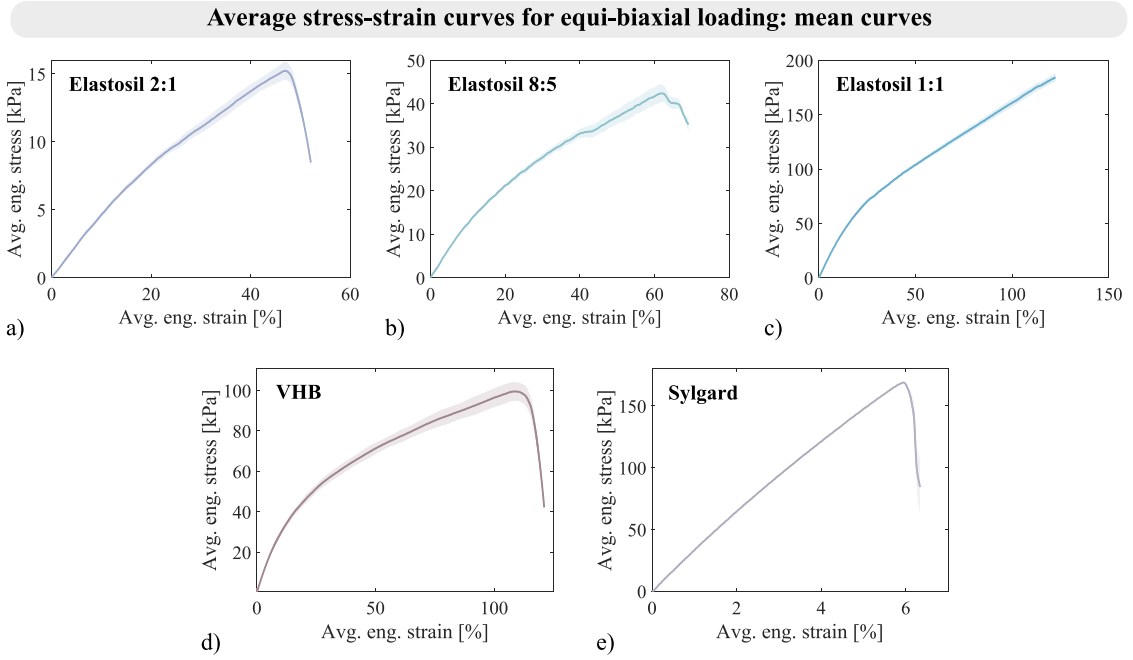

Fig. 2. Experimental results for the biaxial experiments. The two independent axes move identically at a displacement rate of $0.85\,\mathrm{mm\,s^{-1}}$, which renders a strain rate of $0.01\,\mathrm{s^{-1}}$. (a–e) Average engineering stress versus average engineering strain curves for equi-biaxial tensile tests on Elastosil with mixing ratios of 2:1, 8:5, and 1:1, VHB, and Sylgard, respectively. The average engineering strain is obtained dividing the value of displacement of the clamps by the initial distance between clamps (l_0) and the engineering stress is calculated for each axis as force per unit of initial cross-section area. Scatter areas are included to quantify the variation between the measurements of the two independent axes. To compute the scatter areas, the mean force–displacement curves for each axis are first determined. The scatter area is then defined as the region enclosed between these two mean curves. Consequently, it does not capture the variability among individual experimental repetitions, but rather the variability between the already averaged results corresponding to each axis. Four repetitions are performed for the same tests conditions. The curves for the individual experimental repetitions are presented in Fig. A.13.

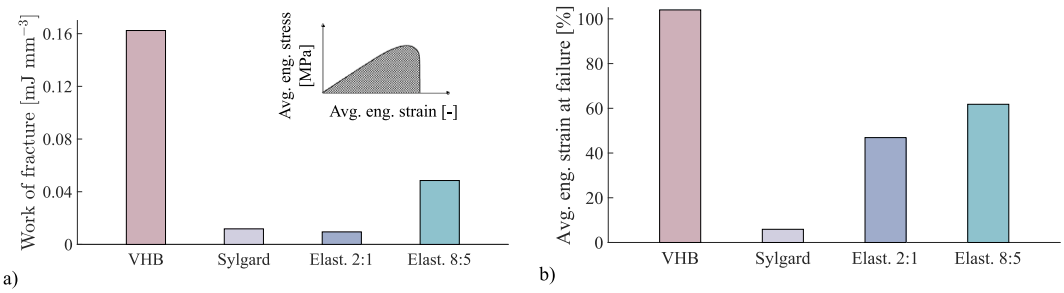

Fig. 3. Experimental total work of fracture and strain at failure for the biaxial experiments. (a) Work of fracture for each material calculated as the total work performed by both axes during the deformation of the sample until full propagation of the crack divided by the initial volume of the sample. The volume of the samples is 85 mm × 85 mm × 2 mm (thickness) for all samples except for VHB. For VHB, thickness is 0.5 mm. Schematic inset: outlines the area under the stress–strain curve used to compute the total work of fracture. (b) Average strain at failure for each elastomer calculated as the displacement for the maximum force. The average engineering strain is obtained dividing the value of displacement of the clamps by the initial distance between clamps (l_0). The values are taken as the displacement for the maximum value of stress of the mean curves. Note that the work of fracture and displacement at failure for Elastosil 1:1 is not included as the samples do not rupture.

Table 1

Experimental results for the average engineering strain at the onset of crack extension. The displacement at crack onset corresponds to the instant when initial crack growth take place—and not when full rupture occurs, which is reported in Fig. 3. The results are identified from the images for the four experimental repetitions (denoted as "Rep."). The mean values and standard deviation for each material are included. The average engineering strain at crack onset is obtained dividing the value of displacement of the clamps by the initial distance between clamps (l_0).

	Rep.	Elastosil 2:1	Elastosil 8:5	Elastosil 1:1	VHB	Sylgard
Average eng. strain at crack onset [%]	1	18.4	42.7	32.4	50.0	7.4
	2	43.3	36.6	33.3	76.7	6.1
	3	29.3	33.3	26.0	68.0	6.2
	4	38.4	27.6	31.6	35.1	6.7
		32.4 ± 9.5	35.1 ± 5.5	30.8 ± 2.9	57.5 ± 16.1	6.6 ± 0.5

A critical aspect of the analysis concerns the onset of crack propagation and the corresponding displacement at which it occurs. Distinguishing between the pre-crack and post-crack phases during equi-biaxial deformation is essential[8]: the constitutive models introduced in the following section are calibrated exclusively using data from the pre-crack regime, and the configurational forces are evaluated precisely at the loading stage where crack propagation initiates. To this end, Table 1 reports the strain values (and Table A.2 the displacement values) at crack onset for each material and for all experimental repetitions. As in previous figures, each repetition is labeled 1 through 4 to facilitate correlation with the raw dataset available on Zenodo. The results are consistent with the trends observed in the strain at failure: VHB exhibits the highest strain at crack onset, reaching 57.5 %, while Sylgard shows the lowest value at 6.6 %. Elastosil 2:1 and Elastosil 8:5 fall in between, with onset strains of 32.4 % and 35.1 %, respectively. The material characterization plays a central role in this work, since accurately capturing the constitutive behavior of soft elastomers from experimental data is essential for the reliable application of the Configurational Force Method to soft solids.

The fracture typology also varies across materials. VHB, Sylgard, and Elastosil 2:1 and Elastosil 8:5 exhibit forward fracture while Elastosil 1:1 undergoes sideways fracture. As previously reported by the authors (Moreno-Mateos and Steinmann, 2024b), high degrees of crosslinking lead to deformation-induced fracture anisotropy, whereby cracks tend to propagate parallel to the direction of maximum stretch. Supplementary Video 1 illustrates this mechanism for one of the Elastosil 1:1 experiments—an elastomer characterized by high crosslink density and sideways fracture behavior. Interestingly, Elastosil 1:1 fails at a lower strain than its less crosslinked counterparts, with a crack onset strain of only 30.8 % (see Table 1). This indicates that sideways cracks initiate earlier compared to forward cracks observed in the 2:1 and 8:5 variants. However, the extreme stretchability afforded by the sideways fracture mechanism prevents full rupture, allowing the material to accommodate large deformations without complete failure.

Until now, the discussion has focused on the average strain experienced by the samples. However, the local deformation near the central notch offers additional insight into the fracture behavior. To explore this, we use DIC to analyze the strain fields in the vicinity of the crack tip. Fig. 4 presents the full-field strain maps at the onset of crack extension (cf. Table 1) for experimental repetition 1 across all materials. The corresponding strain fields for repetitions 2, 3, and 4 are provided in Appendix B (Figs. B.14–B.16). Consistent with the global metrics discussed earlier (total work of fracture and average strain at failure), VHB exhibits the highest

[8] The displacement for crack onset for each material was determined by visually inspecting the high-frequency image sequences recorded during the experiments. This allowed to reliably identify both the onset of cracking and the fracture topology. While this manual approach may be time-consuming for larger datasets, it was adequate for the scope of our study.

local strains at the onset of crack extension, reaching values of 100 % in both ϵ_{xx} and ϵ_{yy}.[9] The shear component ϵ_{xy} peaks at 55 %. In contrast, Sylgard shows the lowest crack-tip strains, with peak values of 15 % for ϵ_{xx} and ϵ_{yy}, and 10 % for ϵ_{xy}. Notably, the ratio $\epsilon_{xy}/\epsilon_{xx/yy}$ is higher for Sylgard than for VHB. This is attributed to the sharper crack geometry in Sylgard resulting from it higher stiffness, which concentrates strain more intensely compared to the blunter, more rounded cracks seen in Elastosil and VHB, where large deformations cause the crack to evolve into a circumferential-like cavity. For the Elastosil materials, the low-crosslinked version (Elastosil 2:1) reaches strain values of 78 % in ϵ_{xx} and ϵ_{yy}, and 30 % in ϵ_{xy}. The intermediate-crosslinked variant (Elastosil 8:5) displays slightly higher values: 85 %, 85 %, and 34 %, respectively. Finally, the highly crosslinked formulation (Elastosil 1:1), which undergoes sideways fracture, exhibits strains of 73 % (ϵ_{xx}), 70 % (ϵ_{yy}), and 34 % (ϵ_{xy}). As discussed previously, these comparatively lower values can be explained by the earlier onset of crack propagation in Elastosil 1:1. Nonetheless, the sideways fracture mechanism permits large deformations without complete rupture. In summary, the local strain fields offer valuable insight into the distribution and concentration of deformation at the crack tip. However, they are insufficient to fully describe the material's mechanical response, particularly in terms of stress. To address this, the next section introduces a data-adaptive framework for hyperelastic energy functions capable of capturing the stress–strain behavior underlying the observed deformation patterns for different soft constitutive behaviors.

3. Data-adaptive hyperelastic constitutive modeling

Our framework for data-adaptive-based configurational forces for fracture is built on two key pillars: (i) a data-adaptive framework for hyperelastic energy functions and (ii) the Configurational Force Method, implemented as a postprocessing algorithm. The present section sets the stage building up on the data-adaptive framework developed by the authors that captures the constitutive behavior with sufficient accuracy (see seminal works Wiesheier et al., 2023, 2024) — because accurately capturing the constitutive behavior of soft solids is key for a reliable application of the Configurational Force Method to soft solids. In this regard, some challenges were outlined by the authors in Moreno-Mateos and Steinmann (2024a). The framework integrates reaction force measurements from the testing machine with displacement fields obtained via DIC, and remains robust even when the DIC data is spatially incomplete, i.e., limited to a region of interest (ROI).[10] Fig. 5 provides an overview of the methodology. The hyperelastic strain energy functions will be eventually used in the calculation of the Eshelby stress tensor in the Configurational Force Method. Our FEMU optimization strategy requires the repeated solution of the mechanical boundary-value problem (forward problem), derived succinctly in the following.

3.1. Forward problem: kinematics, strain energy density, stress tensor, FE-implementation

In finite deformation theory, a generic point $\mathbf{X} \in \mathscr{B}_0$ in the material configuration $\mathscr{B}_0$ is mapped to the deformed configuration $\mathscr{B}$ via the deformation map $\boldsymbol{\varphi}$, i.e., $\mathbf{x} = \boldsymbol{\Phi}(\mathbf{X})$. The gradient of the mapping with respect to the material coordinates is defined as the second-order deformation gradient tensor

$$\mathbf{F} = \frac{\partial \mathbf{x}}{\partial \mathbf{X}}, \qquad J = \det \mathbf{F} > 0, \tag{1}$$

where J denotes the determinant of the deformation gradient. The deformation is decomposed into volumetric and isochoric contributions[11] according to

$$\mathbf{F} = \hat{\mathbf{F}} \cdot \bar{\mathbf{F}}, \qquad \hat{\mathbf{F}} = J^{-1/3}\mathbf{I}, \qquad \bar{\mathbf{F}} = J^{1/3}\mathbf{F}, \tag{2}$$

with $\mathbf{I}$ denoting the second-order unit tensor. This multiplicative decomposition carries over to the right Cauchy–Green tensor

$$\mathbf{C} = \mathbf{F}^{\mathrm{T}} \cdot \mathbf{F}, \qquad \bar{\mathbf{C}} = J^{-2/3}\mathbf{C}. \tag{3}$$

Per construction, $\det \bar{\mathbf{C}} = 1$, hence, there are only two principal invariants $\bar{I}_1 = \operatorname{tr} \bar{\mathbf{C}}$, $\bar{I}_2 = \operatorname{tr} \operatorname{cof} \bar{\mathbf{C}}$ characterizing the isotropic hyperelastic material response. These invariants serve as arguments of the strain energy density (per unit volume) given by

$$\Psi = \bar{\Psi}(\bar{I}_1, \bar{I}_2) - p[J - 1]. \tag{4}$$

In this expression, p is a Lagrange multiplier and can be interpreted as the hydrostatic pressure. In particular, p is not derived from a volumetric strain energy density, as commonly approached when modeling compressible material behavior. The material

[9] The strain fields display symmetry with respect to the central notch orientation.

[10] Our data-driven hyperelastic energy functions are obtained with a finite element updating method that provides robustness in incorporating information from displacement fields spatially limited. The material parameters in the weak form are fixed and the displacement field is solved. Then, the material parameters are updated to minimize a residual set with the experiments. This residual contains full field data (displacement field) and force–displacement (reaction forces) data.

[11] The reader may note that for a fully incompressible material ($J = 1$), a decomposition of the strain energy function into volumetric and isochoric contributions may not be required. However, in our FE implementation, the Lagrange multiplier p is element-wise constant. Consequently, $J = 1$ can not be perfectly satisfied at every quadrature point. Instead, only the integrated average of J is equal to one for every element, rendering values $J \approx 1$ at the quadrature points. This requires the aforementioned decompositon and the usage of isochoric invariants in our FE implementation.

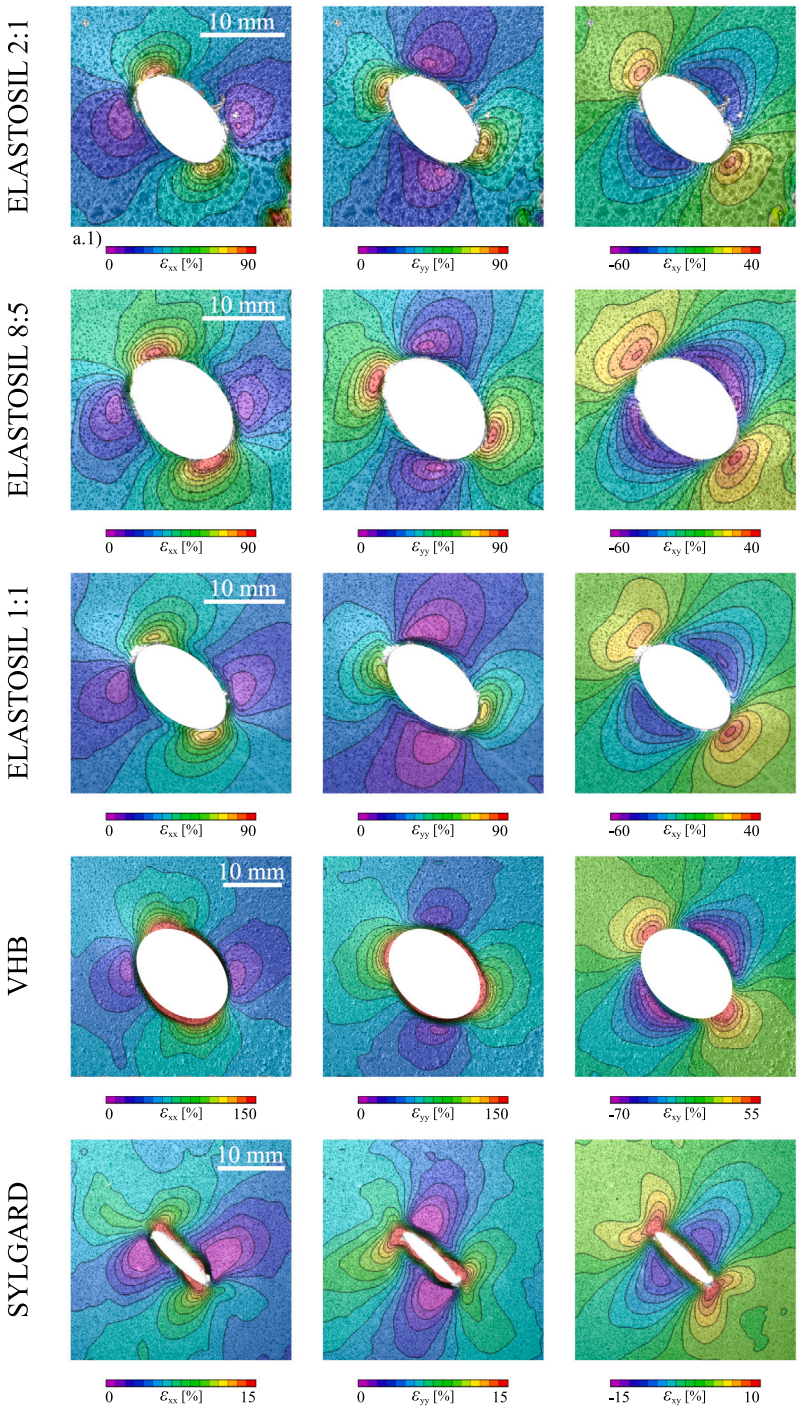

Fig. 4. Strain fields at onset of crack growth for experimental repetition 1. The fields are engineering strain fields computed from the Lagrange strain tensor. The fields correspond to average engineering strains at crack onset of: 18.4 % for Elastosil 2:1, 42.7 % for Elastosil 8:5, 32.4 % for Elastosil 1:1, 50.0 % for VHB, and 7.4 % for Sylgard (see Fig. 2.a–e and Table 1). The fields correspond for Repetition ① (out of the four repetitions performed for the same type of sample and same test conditions). Note that x and y denote the horizontal and vertical directions, respectively. To improve the visual presentation of the results, custom white masks are applied to the regions corresponding to the interior of the deformed cracks.

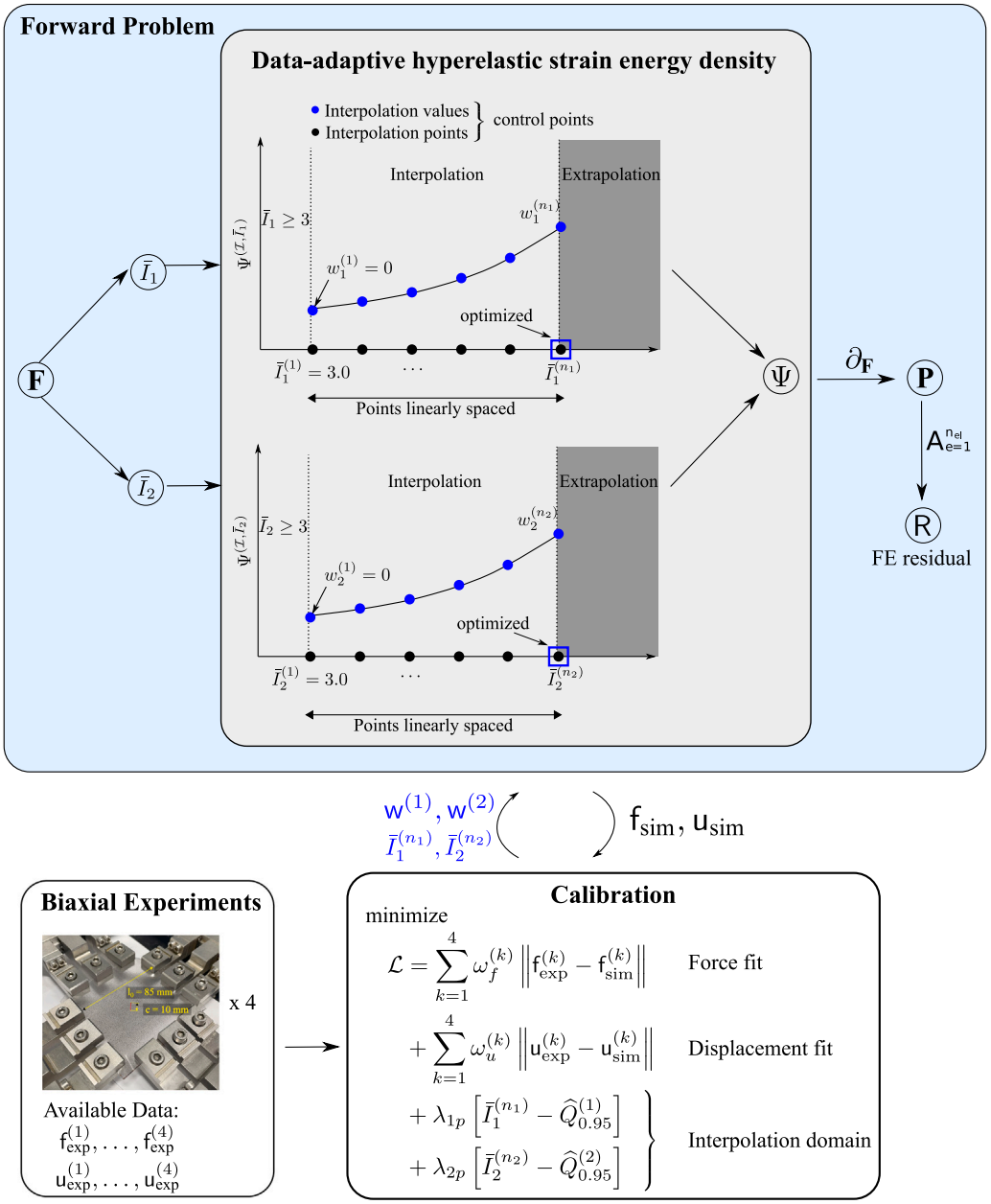

Fig. 5. Schematics of the data-adaptive hyperelastic constitutive modeling framework. The invariants $\bar{I}_1, \bar{I}_2$ are discretized with interpolation points (black circles) and the corresponding interpolation values (blue circles) represent unknown material parameters. Interpolation points and values uniquely define the B-Spline interpolation functions, which, if required, can be extrapolated by continuing the last spline segment. The interpolation values and the interpolation domain are determined via calibration, using global reaction forces and DIC data obtained from biaxial experiments.

must be thermodynamically consistent. This is automatically satisfied when the Piola stress tensor is derived from the strain energy density according to

$$\mathbf{P} = \frac{\partial \bar{\Psi}}{\partial \mathbf{F}} - p\mathbf{F}^{-\mathrm{T}}. \tag{5}$$

Neglecting body forces, the mechanical boundary-value problem has the format

$$\begin{aligned} \mathrm{Div}\,\mathbf{P} &= \mathbf{0} \quad \text{in } \mathscr{B}_0, \\ \det \mathbf{F} - 1 &= 0 \quad \text{in } \mathscr{B}_0, \\ \mathbf{u} &= \widetilde{\mathbf{u}} \quad \text{on } \partial\mathscr{B}_0^{\mathrm{D}}, \\ \mathbf{P}\cdot\mathbf{N} &= \widetilde{\mathbf{T}} \quad \text{on } \partial\mathscr{B}_0^{\mathrm{N}}. \end{aligned} \tag{6}$$

In this formulation there are two equations to be satisfied: $\mathrm{Div}\,\mathbf{P} = \mathbf{0}$, which represents the balance of linear momentum in the material configuration, and $J - 1 = 0$, which accounts for incompressibility of the considered materials. Together, these lead to a mixed FE formulation, where the pressure p and the displacement $\mathbf{u}$ are the primary nodal unknowns. We discretize $\mathbf{u}$ using linear Lagrange polynomials, and p is element-wise constant. As a result, the FE residual vector splits into two blocks: $\mathsf{R} = \left[\mathsf{R}_{\mathbf{u}}, \mathsf{R}_p\right]$. The notation of the FE residual vector is important for the formulation of the optimization problem for calibrating our data-adaptive hyperelastic energy functions, as it will be shown later.

3.2. B-Spline interpolation strain energy density

Since the pressure field p does not originate from a volumetric strain energy density, material parameters are exclusively confined to the isochoric strain energy density. Instead of specifying a canonical model (e.g., Mooney–Rivlin Mooney, 1940 or Yeoh, 1990), we express the isochoric strain energy density using an additive B-Spline interpolation representation,

$$\bar{\Psi}^{(\bar{I}_1,\bar{I}_2)} = \underbrace{\sum_{i=1}^{n_1} c_i^{(1)} B_i^{(1)}(\bar{I}_1)}_{\bar{\Psi}^{(\bar{I}_1)}} + \underbrace{\sum_{j=1}^{n_2} c_i^{(2)} B_j^{(2)}(\bar{I}_2)}_{\bar{\Psi}^{(\bar{I}_2)}}, \tag{7}$$

where $\bar{\Psi}^{(\bar{I}_1)}, \bar{\Psi}^{(\bar{I}_2)}$ are univariate cubic B-Spline functions with control points

$$\mathsf{c}^{(1)} = \left[c_1^{(1)}, \dots, c_{n_1}^{(1)}\right], \quad \mathsf{c}^{(2)} = \left[c_1^{(2)}, \dots, c_{n_2}^{(2)}\right]. \tag{8}$$

Cubic B-Spline basis functions were chosen as the integration into an FE code requires continuous second derivatives of the univariate splines. The splines are constructed from prescribed interpolation points and corresponding interpolation values, see Fig. 5 for a graphical representation on the example of the first invariant $\bar{I}_1$. Specifically, we define

$$\begin{aligned} &\text{Interpolation points:} && \left\{\bar{I}_1^{(i)}\right\}_{i=1}^{n_1}, \quad \left\{\bar{I}_2^{(i)}\right\}_{i=1}^{n_2}. \\ &\text{Interpolation values:} && \mathsf{w}^{(1)} = \left[\bar{\Psi}^{(\bar{I}_1)}(\bar{I}_1^{(i)})\right]_{i=1}^{n_1} = \left[w_1^{(1)}, \dots, w_1^{(n_1)}\right], \\ & && \mathsf{w}^{(2)} = \left[\bar{\Psi}^{(\bar{I}_2)}(\bar{I}_2^{(i)})\right]_{i=1}^{n_2} = \left[w_2^{(1)}, \dots, w_2^{(n_2)}\right]. \end{aligned}$$

This implies that the splines are uniquely defined in terms of the interpolation points and values. The control points, as appearing in Eq. (7), are computed by solving a linear equation system in a pre-processing stage in the forward solve. Computational costs associated with the control point computation are negligible. We refer to d. Boor (1978), Piegl and Tiller (1996) for more insights into splines.

Several requirements must be met to use the splines for describing a hyperelastic material response:

- **Thermodynamic consistency:** $\mathbf{P} = \partial\bar{\Psi}^{(\bar{I}_1,\bar{I}_2)}/\partial\mathbf{F}$.
- **Material frame indifference:** $\bar{\Psi}^{(\bar{I}_1,\bar{I}_2)}(\mathbf{Q}\cdot\mathbf{F}) = \bar{\Psi}^{(\bar{I}_1,\bar{I}_2)}(\mathbf{F}) \quad \forall\, \mathbf{Q} \in \mathrm{SO}(3)$.
- **Material symmetry:** $\bar{\Psi}^{(\bar{I}_1,\bar{I}_2)}(\mathbf{F}\cdot\mathbf{Q}) = \bar{\Psi}^{(\bar{I}_1,\bar{I}_2)}(\mathbf{F}) \quad \forall\, \mathbf{Q} \in \mathrm{SO}(3)$.
- **Positivity:** $\bar{\Psi}^{(\bar{I}_1,\bar{I}_2)} \geq 0 \quad \forall\, \mathbf{F}$.
- **Zero energy undeformed state:** $\bar{\Psi}^{(\bar{I}_1,\bar{I}_2)}(\mathbf{F} = \mathbf{I}) = 0$.

Thermodynamic consistency, material frame indifference (objectivity), and material symmetry are satisfied a priori by (i) deriving the Piola stress from a strain energy density and (ii) parameterizing it in terms of the principal invariants $\bar{I}_1, \bar{I}_2$. Zero energy in the undeformed state can be easily fulfilled by placing the first interpolation points at ($\mathbf{F} = \mathbf{I} \rightarrow \bar{I}_1 = \bar{I}_2 = 3.0$) and fixing the corresponding two interpolation values to zero, i.e.,

$$\bar{I}_1^{(1)} = \bar{I}_2^{(1)} = 3.0, \qquad w_1^{(1)} = w_2^{(1)} = 0. \tag{9}$$

During calibration, this represents a simple bound constraint guaranteed to be satisfied at every iteration. Note that the condition $\mathbf{P}(\mathbf{F}=\mathbf{I})=\mathbf{0}$ is always satisfied due to the choice of isochoric invariants $\bar{I}_1, \bar{I}_2$ and does not require any constraints on the energy value Ψ or its partial derivatives $(\mathrm{d}\Psi/\mathrm{d}\bar{I}_1, \mathrm{d}\Psi/\mathrm{d}\bar{I}_2)$ in the undeformed state (cf. Dammaß et al., 2025).

Remark. There is one subtle detail concerning the spline interpolation. While the evaluations of the splines at points inside the interpolation domain are straightforward, the evaluations at points outside the interpolation domain, i.e., out-of-bounds evaluations, need to be adequately addressed. To that end, we implemented a robust extrapolation strategy by continuing the last spline segment. This allows for evaluation at arbitrary points $\bar{I}_1, \bar{I}_2$ in the invariant space, regardless of the interpolation domain. Nevertheless, we want to emphasize that extrapolation should not occur frequently. Hence, it is desirable to tie the interpolation domain to the sampled invariants. This is guaranteed during the calibration stage of our data-adaptive hyperelastic energy functions, discussed in the following.

3.3. Material model calibration (inverse problem)

The unknown interpolation values $\mathsf{w}^{(1)}, \mathsf{w}^{(2)}$ are determined via non-linear least squares optimization. This procedure requires the repeated solution of the bespoke forward problem until a stopping criterion is met. Our data-adaptive framework leverages full-field displacement fields obtained from DIC and global reaction forces across four experimental repetitions for each material. This comprehensive experimental database motivates the following objective function

$$\mathcal{L} = \sum_{k=1}^{4} \left[\omega_f^{(k)} \|\mathsf{f}_{\mathrm{sim}}^{(k)} - \mathsf{f}_{\mathrm{exp}}^{(k)}\|^2 + \omega_u^{(k)} \|\mathsf{u}_{\mathrm{sim}}^{(k)} - \mathsf{u}_{\mathrm{exp}}^{(k)}\|^2 \right] + \lambda_{1p} \left[\bar{I}_1^{(n_1)} - \widehat{Q}_{0.95}^{(1)} \right] + \lambda_{2p} \left[\bar{I}_2^{(n_2)} - \widehat{Q}_{0.95}^{(2)} \right]. \tag{10}$$

In this objective function, we minimize the discrepancy between experimental and simulated force and displacement data across four experimental repetitions. The first term penalizes differences in the reaction forces while the second term enforces alignment of the displacement fields. The last two terms guide the extend of the interpolation domain for the strain energy function, ensuring that it covers the relevant ranges observed in the simulation. The inclusion of physical quantities with different units (forces and displacements) requires an appropriate weighting strategy. Specifically, the force and displacement contributions of the objective function are weighted according to

$$\omega_f^{(k)} = \frac{1}{\max(\mathsf{f}_{\mathrm{exp}}^{(k)})}, \quad \omega_u^{(k)} = \frac{1}{\max(\mathsf{u}_{\mathrm{exp}}^{(k)})}, \tag{11}$$

where $\omega_f^{(k)}$ and $\omega_u^{(k)}$ are normalization factors ensuring that each term contributes comparably to the objective function regardless of units or magnitudes. The vector $\mathsf{f}_{\mathrm{exp}}^{(k)}$ contains measured reaction forces at multiple loading stages of the clamps, extracted from the curves showcased in Fig. A.13, and the simulation counterpart $\mathsf{f}_{\mathrm{sim}}^{(k)}$ represents the numerical reaction force at the equivalent load step in the forward model. For the displacement data, the full-field displacement fields are first bilinearly interpolated onto the nodes of the employed FE mesh using the `ResampleWithDataset` filter (available in Paraview). The interpolated displacements are then evaluated at identification nodes defined within a Region of Interest (ROI) near the crack (cf. Fig. 6 for a qualitative illustration), effectively downsampling the displacement fields for the calibration. These identification nodes were selected consistently across all four experimental repetitions and clamp loading stages. That is, the material coordinates of the incorporated identification nodes remain identical across repetitions and loading stages. Finally, the downsampled displacements across the loading stages are assembled into the vector $\mathsf{u}_{\mathrm{exp}}^{(k)}$, and $\mathsf{u}_{\mathrm{sim}}^{(k)}$ denotes the corresponding displacements predicted by the simulation.

Aside from the choice of experimental data for the calibration, another important detail of the calibration is the definition of the interpolation domain for the interpolation functions $\bar{\Psi}^{(I,\bar{I}_1)}$ and $\bar{\Psi}^{(I,\bar{I}_2)}$. During the forward problem, the splines are evaluated at the invariant values at the quadrature points. However, these evaluation points are unknown before the calibration and are implicitly defined by the deformation gradient. This impedes the definition of fixed interpolation points and suggests considering the interpolation domains underlying $\bar{\Psi}^{(I,\bar{I}_1)}$ and $\bar{\Psi}^{(I,\bar{I}_2)}$ also as unknown. To simplify the treatment of the interpolation domains during the calibration, we expand the parameter space by treating only the last interpolation points $\bar{I}_1^{(n_1)}, \bar{I}_2^{(n_2)}$ as additional optimization variables, and linearly re-distributing the remaining interpolation points, see Fig. 5. This ensures that the interpolation domain aligns well with the sampled invariants, but necessitates the inclusion of two additional loss terms to drive $\bar{I}_1^{(n_1)}, \bar{I}_2^{(n_2)}$ towards the sampled invariant space, approximated by the 95th-percentiles $\widehat{Q}_{0.95}^{(j)}$, obtained from Kernel Density estimation (KDE).[12] More details on KDE are presented in Appendix C.

[12] The values λ_{1p} and λ_{2p} are weighting factors that control the alignment of $\bar{I}_1^{(n_1)}$ and $\bar{I}_2^{(n_2)}$ with the KDE-approximated 95th percentiles $\widehat{Q}_{0.95}^{(1)}$ and $\widehat{Q}_{0.95}^{(2)}$, respectively.

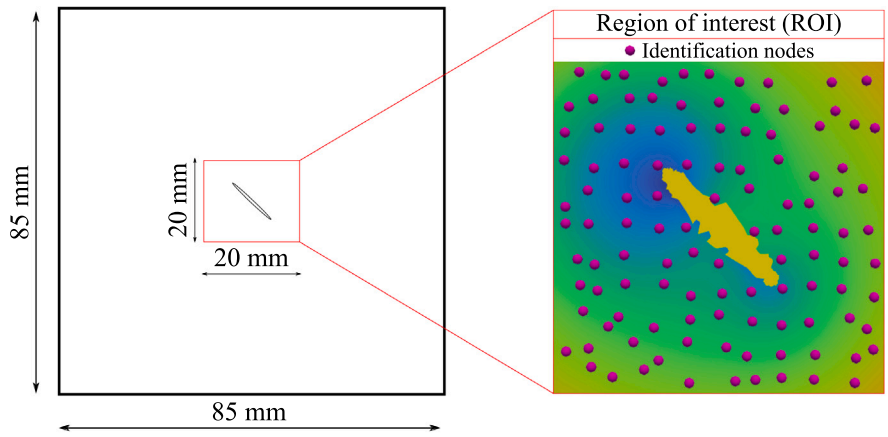

Fig. 6. Region of interest used to sample the experimental displacement fields to the FE mesh and calibrate data-adaptive strain energy functions. A square region of interest (ROI) with dimensions 20 mm × 20 mm in the vicinity of the crack contour is defined. The ROI is chosen consistently for each material, except for Elastosil 8:5, where the ROI has dimensions 17 mm × 17 mm. For the material model calibration, the DIC information is restricted to the highlighted identification nodes within the ROI. These were obtained by defining 10 × 10 evenly distributed sampling points in the ROI and finding the closest node of the FE mesh for each sampling point. The resulting FE mesh nodes define the set of identification nodes. The yellow-colored area in the center of the ROI indicates missing DIC data — this area can be different for each repetition.

We denote the complete set of calibration parameters as θ, comprising the interpolation values and endpoints for the interpolation domains of the first and second invariant. Eventually, the parameter optimization problem has the following format

$$\begin{aligned} \theta &= \left[\mathrm{w}^{(1)},\ \mathrm{w}^{(2)},\ \bar{I}_1^{(n_1)},\ \bar{I}_2^{(n_2)}\right], \\ \theta^* &= \underset{\theta\in\mathbb{R}^{n_1+n_2+2}}{\arg\min}\ \mathcal{L}, \\ \text{subject to}\quad & \frac{\mathrm{d}^2\bar{\Psi}^{(I,\bar{I}_1)}}{\mathrm{d}\bar{I}_1^2} \geq 0, \\ & \frac{\mathrm{d}^2\bar{\Psi}^{(I,\bar{I}_2)}}{\mathrm{d}\bar{I}_2^2} \geq 0, \\ & \mathsf{R}(\theta) = 0. \end{aligned} \tag{12}$$

The constraints in the optimization ensure physical plausibility: convexity of the strain energy function with respect to the invariants,[13] and satisfaction of equilibrium via the finite element residual $\mathsf{R}(\theta)$. The positivity of the second derivatives with respect to the invariants constitutes a set of nonlinear inequality constraints, handled by the optimization solver with Lagrange multipliers. Conversely, $\mathsf{R}(\theta) = 0$ ensures that the equilibrium conditions (weak form of the balance of linear momentum, incompressibility) are satisfied, achieved by a forward simulation with the current values of the calibration parameters θ. We solve this constrained optimization problem using *fmincon*, the nonlinear programming solver provided by *MATLAB*. At every iteration, the objective function is evaluated by calling our in-house forward solver based on the `deal.II` library (Arndt et al., 2022, 2021). The optimization terminates when the relative change in either the objective function value or the parameter step size between successive iterations falls below the tolerance 1×10^{-12}.

3.4. Discovered material models

Figs. 7, 8, 9, 10 and 11 summarize the results for the materials Elastosil 2:1, Elastosil 8:5, Elastosil 1:1, Sylgard, and VHB, respectively. Each figure follows a consistent layout and includes: (a) the identified strain energy density, (b) a comparison between the numerical and experimental reaction forces, and the error between numerical and experimental displacement fields in both (c) horizontal and (d) vertical directions.

Our data-adaptive framework for hyperelastic energy functions leverages both reaction forces data and full-field displacement measurements from DIC to optimize the energy functions. To ensure accuracy, the discrepancies between experimental and computational data — both in terms of reaction forces and displacement fields — must be inspected. We use the identified strain

[13] We emphasize that, unlike $\bar{I}_1$, the invariant $\bar{I}_2$ is not polyconvex (Ball, 1976). Consequently, enforcing the condition $\mathrm{d}^2\Psi/\mathrm{d}\bar{I}_2^2 \geq 0$ does not ensure polyconvexity. Since our identified data-adaptive hyperelastic energy functions depend solely on $\bar{I}_1$, the implemented constraint $\mathrm{d}^2\Psi/\mathrm{d}\bar{I}_1^2 \geq 0$ suffices to guarantee polyconvexity.

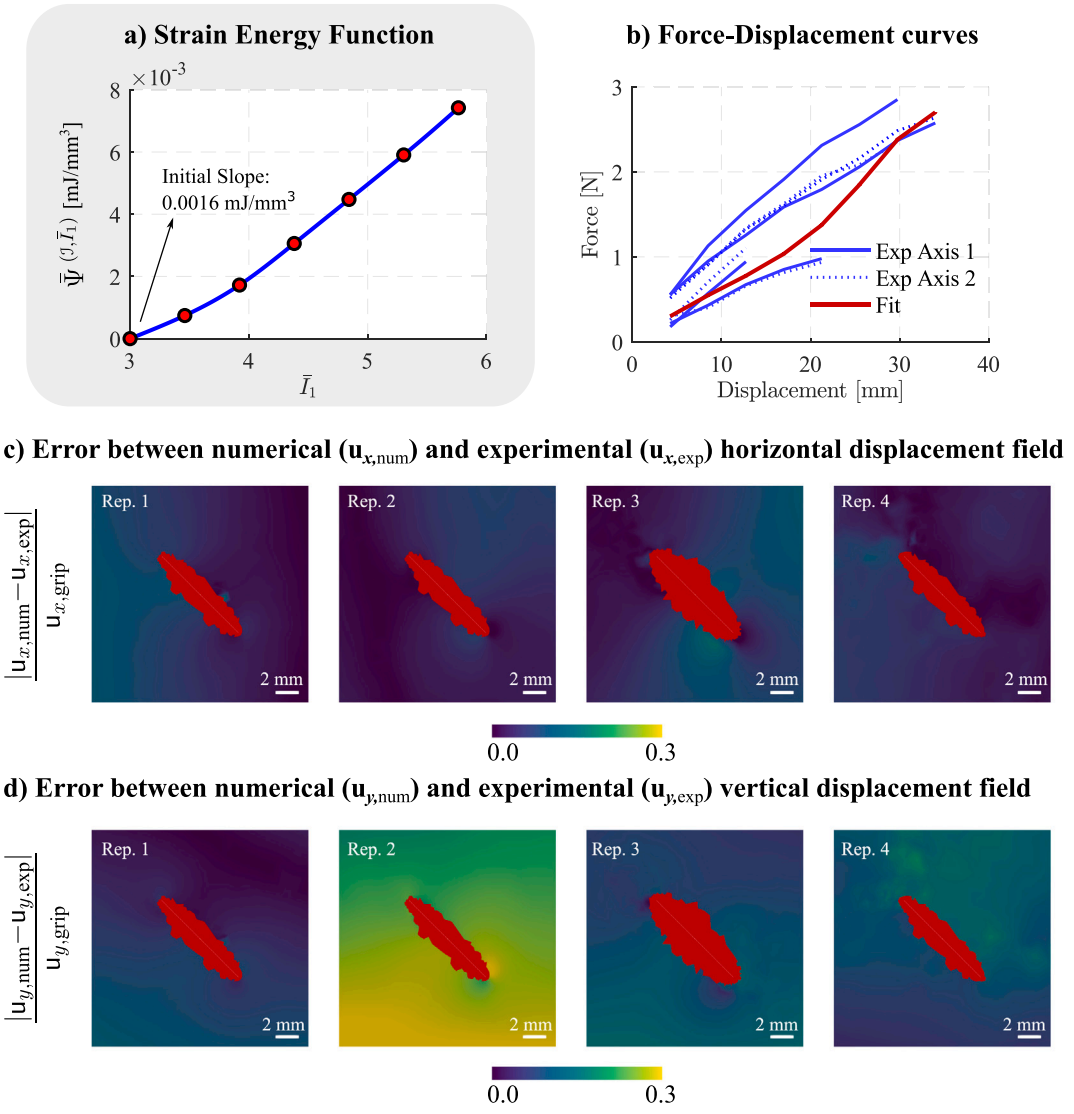

Fig. 7. Data-adaptive strain energy function for Elastosil 2:1 obtained from biaxial experimental data: reaction forces and full-field DIC measurements. (a) Data-adaptive hyperelastic strain energy density as a function of the first invariant, $\bar{I}_1$. The energy function is reconstructed as a linear combination of control points defined in the invariant space and B-spline basis functions (see Eq. (7)), with a maximum value of $\bar{I}_1$ of 5.76. (b) Comparison between experimental and numerically fitted reaction forces at the clamps, plotted against the displacement of the biaxial testing machine's actuators (total displacement per axis). (c) Normalized error in the horizontal displacement field within the region of interest — specifically the crack and crack-tip vicinity (cf. Fig. 6) — across four experimental repetitions under identical loading conditions. Displacement of the grips is used as the normalization reference. (d) Relative error in the vertical displacement field for the same region of interest and experimental repetitions as in (c), using the same normalization convention.

energy densities to solve the forward problem and obtain the numerical reaction force (see Figs. 7–11.b). While the experimental data comprises eight curves — four repetitions and two axes —, there is only a single numerical prediction (solid red line). The numerical reaction force consistently falls within the scatter of the experimental data, indicating good average agreement. For Elastosil 2:1, it is noteworthy that the predicted reaction force shown in Fig. 7 reflects the scatter observed in the experimental force–displacement curves, particularly in terms of the maximum displacement. As a result, at large displacements, the numerical curve tends to follow the subset of experimental curves that extend to similarly large displacement values. In turn, the bottom panels of the figures show the error between the numerical and experimental displacement field in both horizontal and vertical direction within the ROI defined in Fig. 6. To ensure comparability between materials, the absolute displacement error is normalized by the applied grip displacement. The red ellipsoidal regions near the center of the contour plots correspond to areas where DIC data is unavailable; these regions vary across repetitions. While some contours display larger errors, the error remains close to zero for most of the contours, including near the crack tip.

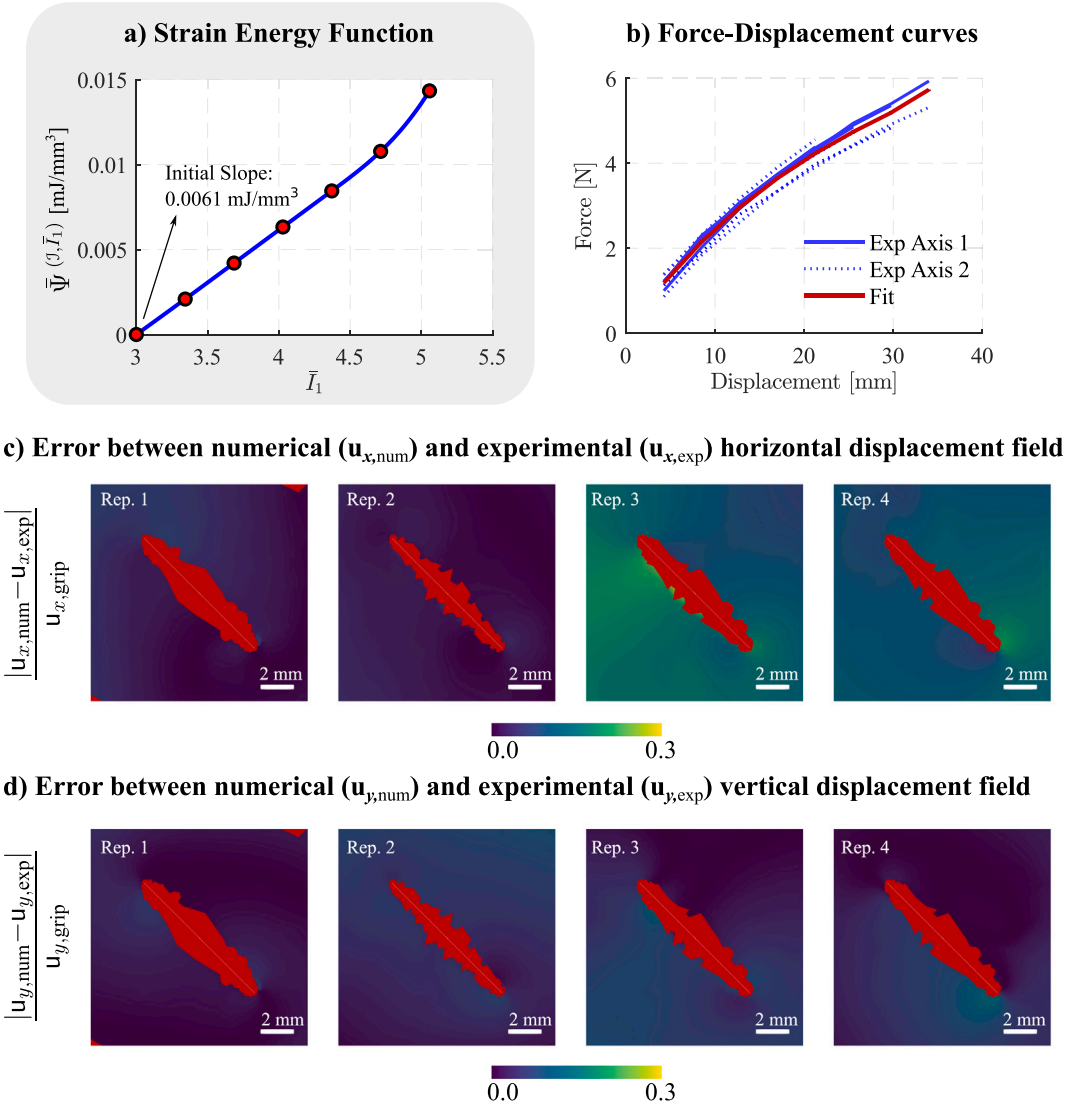

Fig. 8. Data-adaptive strain energy function for Elastosil 8:5 obtained from biaxial experimental data: reaction forces and full-field DIC measurements. (a) Data-adaptive hyperelastic strain energy density as a function of the first invariant, $\bar{I}_1$. The energy function is reconstructed as a linear combination of control points defined in the invariant space and B-spline basis functions (see Eq. (7)), with a maximum value of $\bar{I}_1$ of 5.06. (b) Comparison between experimental and numerically fitted reaction forces at the clamps, plotted against the displacement of the biaxial testing machine's actuators (total displacement per axis). (c) Normalized error in the horizontal displacement field within the region of interest — specifically the crack and crack-tip vicinity (cf. Fig. 6) — across four experimental repetitions under identical loading conditions. Displacement of the grips is used as the normalization reference. (d) Relative error in the vertical displacement field for the same region of interest and experimental repetitions as in (c), using the same normalization convention.

The data-adaptive optimization of the hyperelastic energy functions based on biaxial test data primarily activates the first invariant strain energy function, $\bar{\Psi}^{(I,\bar{I}_1)}$. As outlined in the previous section, we assume an isochoric strain energy density that depends on the invariants $\bar{I}_1$ and $\bar{I}_2$. During optimization, the optimizer consistently deactivated the $\bar{I}_2$ contribution by setting all interpolation values ($w_2^{(j)}$) to their prescribed lower bound of zero.[14] This results in a reduced model depending solely on $\bar{I}_1$. We refer to Appendix D for an extended investigation on the invariants. Across all materials, the condition of zero energy in the

[14] In mathematical terms, $w_2^{(j)} = 0$ indicates that the Lagrange multipliers associated with the lower bound constraints are active at the solution. This means the optimizer would have preferred a solution with $w_2^{(j)} < 0$, but such values are not allowed because the strain energy contribution associated with $\bar{I}_2$ must remain non-negative.

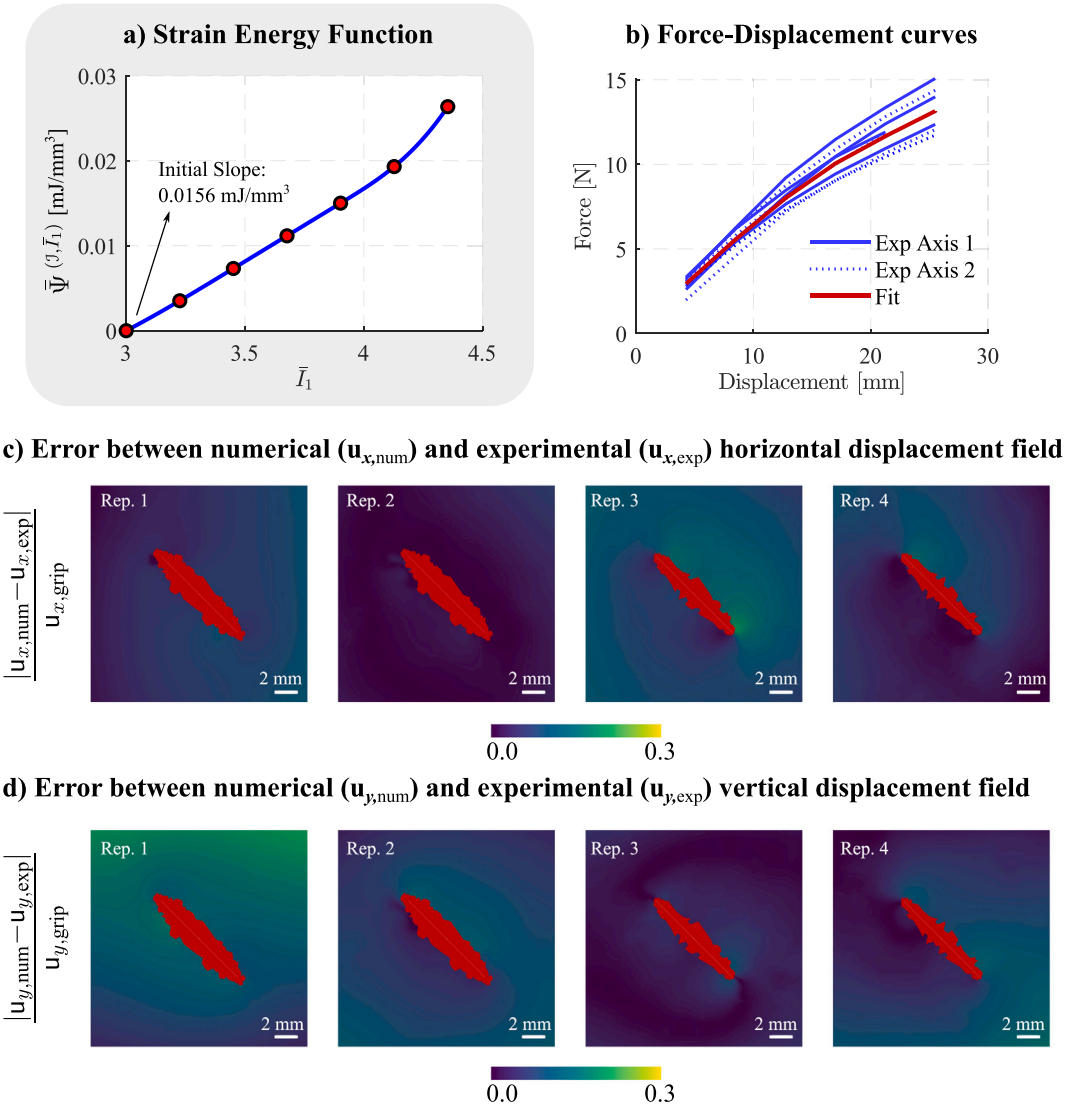

Fig. 9. Data-adaptive strain energy function for Elastosil 1:1 obtained from biaxial experimental data: reaction forces and full-field DIC measurements. (a) Data-adaptive hyperelastic strain energy density as a function of the first invariant, $\bar{I}_1$. The energy function is reconstructed as a linear combination of control points defined in the invariant space and B-spline basis functions (see Eq. (7)), with a maximum value of $\bar{I}_1$ of 4.35. (b) Comparison between experimental and numerically fitted reaction forces at the clamps, plotted against the displacement of the biaxial testing machine's actuators (total displacement per axis). (c) Normalized error in the horizontal displacement field within the region of interest — specifically the crack and crack-tip vicinity (cf. Fig. 6) — across four experimental repetitions under identical loading conditions. Displacement of the grips is used as the normalization reference. (d) Relative error in the vertical displacement field for the same region of interest and experimental repetitions as in (c), using the same normalization convention.

undeformed state is satisfied, i.e, $\bar{\Psi}^{(I,\bar{I}_1)}(\bar{I}_1 = 3.0)$, and the interpolated curves are convex in the interpolation domain. Dammaß and co-authors (Dammaß et al., 2025) recently concluded that "models based solely on $\bar{I}_1$ can make sound predictions for multiaxial loadings even if parameterized only from uniaxial data" and that "$\bar{I}_2$-only models are completely incapable in even qualitatively capturing experimental stress data at large deformations". In line with these findings, the optimizer in our framework for data-driven hyperelastic energy is parsimonious, identifying $\bar{I}_1$-only-based energy functions as sufficient for accurate modeling. We acknowledge, however, that this conclusion is *ad hoc* for our distinct data-driven optimization methodology and experimental dataset on samples with the initial central pre-cut as strain concentrator. The constitutive behavior of our experimental data is sufficiently well described by $\bar{I}_1$ and it might be that $\bar{I}_2$ slightly enhances the model performance for larger stretches.

The different fracture toughness and constitutive behavior of the elastomers yield different deformation states for crack onsets, which limits the interpolation domain for $\bar{I}_1$. The interpolation domain varies across materials, as seen in Figs. 7, 8, 9, 10, and 11.

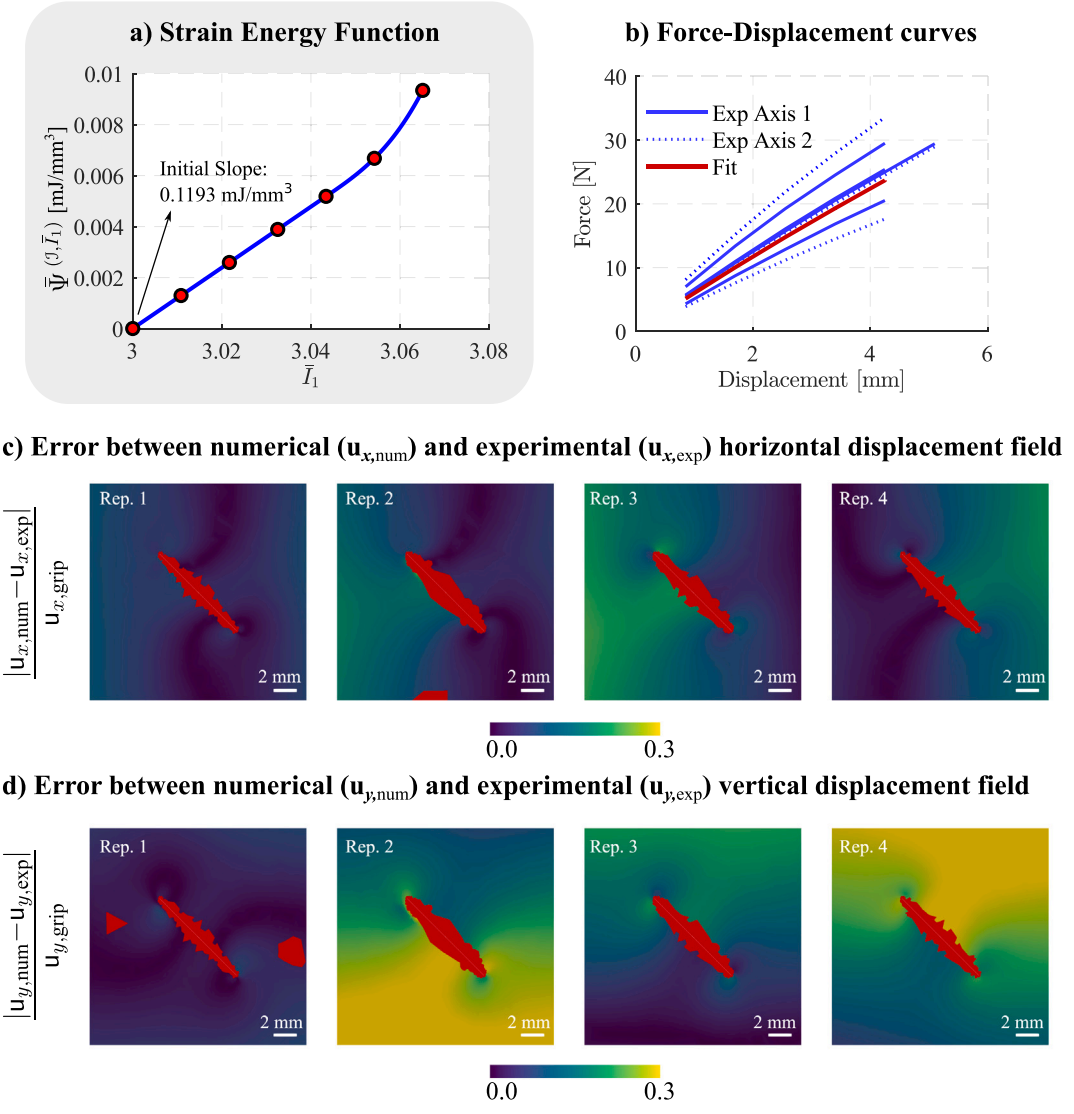

Fig. 10. Data-adaptive strain energy function for Sylgard obtained from biaxial experimental data: reaction forces and full-field DIC measurements. (a) Data-adaptive hyperelastic strain energy density as a function of the first invariant, $\bar{I}_1$. The energy function is reconstructed as a linear combination of control points defined in the invariant space and B-spline basis functions (see Eq. (7)), with a maximum value of $\bar{I}_1$ of 3.07. (b) Comparison between experimental and numerically fitted reaction forces at the clamps, plotted against the displacement of the biaxial testing machine's actuators (total displacement per axis). (c) Relative error in the horizontal displacement field within the region of interest — specifically the crack and crack-tip vicinity (cf. Fig. 6) — across four experimental repetitions under identical loading conditions. Displacement of the grips is used as the normalization reference. (d) Normalized error in the vertical displacement field for the same region of interest and experimental repetitions as in (c), using the same normalization convention.

Sylgard exhibits the smallest interpolation domain, with a maximum value of $\bar{I}_1$ of 3.07, while VHB has the largest value, i.e., 9.77. For the three versions of Elastosil—2:1, 8:5, and 1:1— the values are 5.76, 5.06, and 4.35, respectively. This is consistent with the experimental findings, namely the average strains at crack onset, i.e., 6.6 % for Sylgard, 57.5 % for VHB, 32.4 % for Elastosil 2:1, and 35.1 % for Elastosil 8:5. As discussed, no average strain at crack onset is available for Elastosil 1:1. This demonstrates the adaptability of our model in aligning the interpolation domain with the loading regimes encountered in the experiments.

The data-adaptive hyperelastic energy functions adjust both their values and curvature to accurately reflect the distinct constitutive behaviors of the five soft elastomers studied. The identified functions $\bar{\Psi}^{(\mathcal{I},\bar{I}_1)}$ exhibit an initial linear increase, followed by a gradual increase in curvature toward the upper end of the domain. However, the slope and the curvature evolution differ significantly across the materials. Sylgard, being the most brittle material, exhibits the highest initial slope value (0.1193 N mm^{-2}), followed by VHB (0.0115 N mm^{-2}) and Elastosil 1:1 (0.0156 N mm^{-2}). The lowest values are observed for Elastosil 2:1 and Elastosil 8:5,

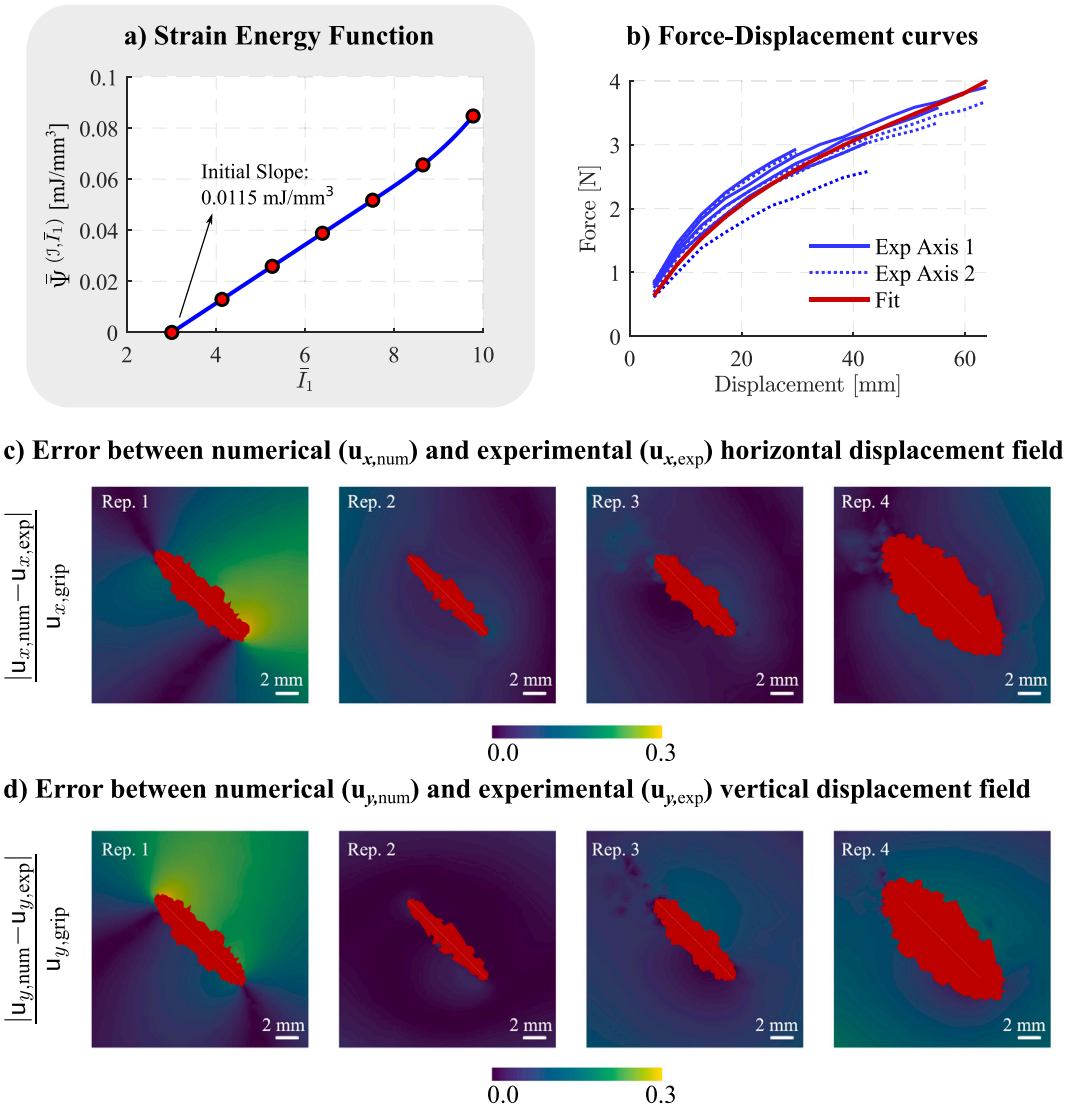

Fig. 11. Data-adaptive strain energy function for VHB obtained from biaxial experimental data: reaction forces and full-field DIC measurements. (a) Data-adaptive hyperelastic strain energy density as a function of the first invariant, $\bar{I}_1$. The energy function is reconstructed as a linear combination of control points defined in the invariant space and B-spline basis functions (see Eq. (7)), with a maximum value of $\bar{I}_1$ of 9.77. (b) Comparison between experimental and numerically fitted reaction forces at the clamps, plotted against the displacement of the biaxial testing machine's actuators (total displacement per axis). (c) Relative error in the horizontal displacement field within the region of interest — specifically the crack and crack-tip vicinity (cf. Fig. 6) — across four experimental repetitions under identical loading conditions. Displacement of the grips is used as the normalization reference. (d) Normalized error in the vertical displacement field for the same region of interest and experimental repetitions as in (c), using the same normalization convention.

with 0.0016 N mm^{-2} and 0.0061 N mm^{-2}, respectively. Although these values cannot be directly interpreted as conventional material parameters such as Young's modulus, they can be related to the shear modulus under the assumption of a neo-Hookean material model. In this context, the (initial) slope of the strain energy function provides an estimate of the shear modulus, with the slope being half the shear modulus.[15] Furthermore, the hyperelastic strain energies reveal the larger strain hardening for Elastosil 8:5 and

[15] Readers interested in the shear modulus for Elastosil in its different crosslinked variants may benchmark the results presented in this paper against the experimental uniaxial tensile data reported in the authors' previous work (Moreno-Mateos and Steinmann, 2024b), albeit the reported metric there was the Young's modulus rather than the shear modulus. The results are consistent and further validate the initial slopes of the strain energy functions in this work. When it comes to Sylgard, the work in Moučka et al. (2021) can be consulted to verify that our calculated shear modulus lies slightly below the experimental

1:1, as well as for Sylgard, with an increase in the curvature on the upper limit of the $\bar{I}_1$ interpolation domain. Overall, our data-adaptive framework for hyperelastic energy functions demonstrates versatility in capturing biaxial experimental responses across soft materials with varying stiffness and distinct hyperelastic behaviors. This is paramount because accurately capturing the constitutive behavior of soft elastomers is key for a reliable application of the Configurational Force Method to soft solids.

4. Configurational force method describes fracture onset under biaxial loading

The framework for data-adaptive configurational forces in fracture mechanics is built upon two core components: (i) a data-adaptive formulation of hyperelastic energy functions, and (ii) the Configurational Force Method, implemented as a post-processing algorithm. The following section addresses point (ii) using a postprocessing algorithm that computes the Eshelby stress tensor and the associated nodal forces—namely, the configurational forces. We set a computational testbed to compute configurational forces in virtual experiments that mimic the actual biaxial tests. The crack tip configurational force will be a computationally efficient estimate of the contour J-integral.

4.1. The configurational force method

The kinematic description of a continuum involves establishing a relationship between the positions of physical points before and after the application of load. The parametrization of the kinematic and energetic quantities in terms of the material positions is commonly known as *spatial motion problem* or rather as *deformational mechanics*. In the *material motion problem* or rather *configurational mechanics*, the kinematic and constitutive measures are parameterized in terms of the spatial positions of the continuum via the inverse deformation gradient.

Just as spatial forces are associated with the deformation of the continuum, configurational forces drive changes in the material configuration, leading to an associated release of energy. The definition of a stress–energy tensor in the material motion description is in the heart of the theory. Akin to the energy density $\Psi^{(I,\bar{I}_1,\bar{I}_2)}(\mathbf{F};\mathbf{X})$ defined in $\mathscr{B}_0$, an energy density $\psi = \psi(\mathbf{f},\boldsymbol{\phi})$, with $\mathbf{f}$ the inverse deformation gradient and ϕ the mapping function $\mathbf{X} = \boldsymbol{\phi}(\mathbf{x})$ from spatial to material coordinates, can be re-defined per unit volume in $\mathscr{B}$, so that $\Psi \simeq [\det \mathbf{F}]\,\psi$. This new energy density serves as a potential for the Eshelby stress tensor (Eshelby, 1951; Kienzler and Herrmann, 1997) in the material configuration through a push-back operation or, alternatively, in the form of the Eshelby energy–momentum tensor (Eshelby, 1975) as a function of the direct deformation gradient (Eshelby, 1999),

$$\boldsymbol{\Sigma}(\mathbf{F}) = \left[\bar{\Psi}^{(I,\bar{I}_1,\bar{I}_2)}\left(\overline{\mathbf{F}}\right) - p\,[\det \mathbf{F} - 1]\right]\mathbf{I} - \mathbf{F}^{\mathrm{T}} \cdot \left[\frac{\partial \bar{\Psi}^{(I,\bar{I}_1,\bar{I}_2)}\left(\overline{\mathbf{F}}\right)}{\partial \mathbf{F}} - p\mathbf{F}^{-\mathrm{T}}\right]. \tag{13}$$

Remark. The energy–momentum representation in Eq. (13) allows to calculate the Eshelby stress via post processing based on the solution of the spatial motion problem.

The material motion problem can be discretized via FE to obtain configurational forces at the nodes of the discretization by elements in $\mathcal{B}_e \in \mathscr{B}_0$ (Steinmann et al., 2001). The configurational force at global node A can be calculated using the material gradient of the global node A basis function (N^A),[16] the Eshelby stress tensor ($\boldsymbol{\Sigma}$), and the FE assembly operator $\mathop{\mathbf{A}}_{e=1}^{n_{\mathrm{el}}}$ over all elements

$$\mathbf{F}^A_{\mathrm{CNF}} = \mathop{\mathbf{A}}_{e=1}^{n_{\mathrm{el}}} \int_{\mathcal{B}_e} \boldsymbol{\Sigma} \cdot \nabla_0 N^A \mathrm{dV}. \tag{14}$$

Remark. Eq. (14) is grounded on a variational statement of configurational balance: the configurational stress acting within each finite element (interpreted as "internal forces") must equilibrate with the configurational forces acting at the element nodes ("external forces"). This balance leads directly to the volume integral shown in Eq. (14), where the gradients of the global basis functions are employed to relate the Eshelby stress tensor to nodal configurational forces.

In consistency with the balance of configurational tractions on a *Pacman-shaped* domain enclosing the crack tip and its vicinity (cf., e.g., Moreno-Mateos and Steinmann, 2024a), our approximation of the J-integral is obtained by summing the spurious configurational forces[17] in a region surrounding the crack tip with the physical configurational forces acting directly at the crack tip (see, e.g., Denzer et al., 2003). To that end, a cylindrical region of radius 0.1 mm is defined to add the spurious forces that lay inside the cylinder close to the crack tip. The size of the cylindrical region is chosen to be sufficiently large to capture all non-negligible spurious forces around the crack tip, while remaining small enough to avoid contributions from the opposite crack tip.

For more details on the motivation and implementation of the Configurational Force Method at finite strains, the reader may consult the dedicated work by the authors, Moreno-Mateos and Steinmann (2024a).

---

values reported by the authors. For uniaxial data of soft elastomers, we also refer to our previous work, including a comprehensive discussion on data-adaptive hyperelastic energy functions (Wiesheier et al., 2024).

[16] The basis functions N^A used to compute nodal configurational forces are equal to the function space used for the Galerkin discretization of the forward problem, i.e., linear Lagrange polynomials.

[17] Spurious nodal configurational forces arise at the crack tip vicinity due to discretization errors, mesh distortion, and numerical artifacts.

4.2. Results

The data-adaptive hyperelastic energy functions identified in the previous section are now incorporated into the Configurational Force Method. Using these functions, both nodal and total configurational forces acting at the crack tip are computed at discrete loading steps throughout the deformation process—prior to crack initiation. The analysis is carried out up to the point at which fracture propagation begins, as determined experimentally from the average displacement at crack onset (see Table A.2). The results, shown in Fig. 12, include: (a) nodal configurational forces at crack onset, (b) evolution of the total configurational force ($\mathbf{F}_{\mathrm{CNF}}$) with clamp displacement, and (c) critical configurational force values at crack onset ($\mathbf{F}_{\mathrm{CNF,C}}$).

A first inspection of the nodal configurational forces at crack onset (Fig. 12.a) shows strong localization of the forces at the nodes at the crack tip edge (physical configurational forces), alongside the presence of minor spurious forces in the vicinity of the tip. The spurious forces are of negligible magnitude. For visual clarity, the arrows depicting these forces are not uniformly scaled across materials and should not be used for quantitative comparison. Nodal configurational forces are, however, a consequence of the FE spatial discretization and, consequently, depend on the FE mesh.

A key quantity of interest is the total crack tip configurational force, ideally expressed per unit thickness, obtained by summing the nodal configurational forces. The total crack tip configurational force provides a direct approximation of the classical contour J-integral. As discussed by the authors in Moreno-Mateos and Steinmann (2024a), the configurational traction forces integrated along a contour enclosing the crack tip — commonly referred to as a *Pacman-shaped* domain — are in equilibrium with the total configurational force acting directly at the crack tip.[18] This balance of configurational forces underpins the theoretical equivalence between the J-integral and the Configurational Force Method. Accurate estimation of the J-integral under the biaxial loading conditions considered here critically depends on capturing the true constitutive response of the soft elastomers. This is effectively achieved through our framework for data-adaptive hyperelastic energy functions, enabling reliable and physically meaningful configurational force predictions.

The evolution of the J-integral, i.e., total configurational force during loading of the samples in the virtual experiments, is closely governed by the non-linear constitutive behavior of each soft elastomer. Quantitative comparability is provided by plotting the magnitude of total configurational force F_{CNF} against grip displacement in Fig. 12.b. This total force is normalized by the initial sample thickness (0.5 mm for VHB, and 2.0 mm for all other materials). Among the materials tested, Sylgard exhibits the steepest increase in F_{CNF}, followed by Elastosil 1:1 and VHB. Elastosil 8:5 and Elastosil 2:1 show the lowest magnitudes. These trends are consistent with the initial slopes of the identified data-adaptive hyperelastic energy functions: highest for Sylgard and lowest for Elastosil 2:1. Overall, the shape of the curves is influenced by both the material's constitutive nonlinearity and the geometric nonlinearities inherent in the experimental setup.

In the spirit of a critical value of the J-integral or stress intensity factor in the context of the rather limited linear elastic fracture mechanics, the total crack tip configurational force at crack onset serves as a measure of the material's fracture toughness. This leads to what we term a configurational-forced-based fracture criterion, in which fracture onset (not complete rupture) is predicted when the magnitude of the total configurational force reaches a critical value, $F_{\mathrm{CNF}} = F_{\mathrm{CNF,C}}$. The bar plot in Fig. 12.c presents the critical configurational forces $F_{\mathrm{CNF,C}}$ for the five soft elastomers investigated in this work. These values correspond to the final points of the force–displacement curves in Fig. 12.b and are as follows: $0.0386\,\mathrm{N\,mm^{-1}}$ for Elastosil 2:1, $0.0994\,\mathrm{N\,mm^{-1}}$ for Elastosil 8:5, $0.2149\,\mathrm{N\,mm^{-1}}$ for Elastosil 1:1, $0.1286\,\mathrm{N\,mm^{-1}}$ for Sylgard, and $0.4228\,\mathrm{N\,mm^{-1}}$ for VHB.[19] These results may be interpreted in relation to the total work of fracture shown in Fig. 3.a. Notably, Sylgard exhibits an intermediate value of $F_{\mathrm{CNF,C}}$ but a remarkably low total work of fracture due to its limited displacement at failure, suggesting a brittle-like fracture behavior. In contrast, VHB displays the highest values of total work of fracture, displacement at failure, and $F_{\mathrm{CNF,C}}$, a hallmark of highly deformable soft elastomers.

Lastly, we write a note on the applicability of the method to the sideways-fracturing Elastosil 1:1 elastomer. Although fracture in this Elastosil variant propagates laterally, the Configurational Force Method predicts a total configurational force vector oriented in the forward-fracturing direction. This apparent inconsistency can be intuitively understood: the outcome stems from the use of an isotropic hyperelastic constitutive model and the underlying variational framework, which, sensu stricto, yields configurational forces pointing in the direction of maximal strain energy release, i.e., the direction in which a virtual crack extension (configurational change) would most efficiently reduce the total energy of the system. As discussed in Moreno-Mateos and Steinmann (2024b), the observed sideways fracture behavior can be explained through deformation-induced fracture anisotropy in elastomers modeled with standard (isotropic) hyperelastic strain energy functions. Within this context, and in the absence of a re-formulated, anisotropy-aware energy density, the Configurational Force Method remains capable of providing a reliable estimate of the magnitude of $\mathbf{F}_{\mathrm{CNF,C}}$, but it falls short in predicting its direction. This limitation arises because the method, as implemented here, does not account for anisotropic fracture resistance — in particular, the fact that the fracture energy is lower in the lateral direction than in the forward direction. A potential remedy here will involve microstructure-informed constitutive models that incorporate complex polymer chain-level mechanisms and their influence on fracture behavior. Readers interested in this direction may consult relevant literature, including (Stumpf et al., 2010; Behnke et al., 2018; Mulderrig et al., 2021; Arunachala et al., 2024; Mulderrig et al., 2025).

[18] As discussed earlier, the nodal configurational forces within a cylindrical region of radius 0.1 mm, centered at the crack tip edge, were summed to compute the total crack tip configurational force. We verified that the choice of radius has only a minor influence on the result. For an exemplary clamp displacement of 42.5 mm in the case of VHB, the total crack tip configurational forces obtained for radii of 0.1 mm, 1.0 mm, and 2.0 mm were $0.3683\,\mathrm{N\,mm^{-1}}$, $0.3511\,\mathrm{N\,mm^{-1}}$, and $0.3545\,\mathrm{N\,mm^{-1}}$, respectively.

[19] We note that $F_{\mathrm{CNF,C}}$ for VHB yields a value approximately twice as large as that reported in Moreno-Mateos and Steinmann (2024a). This discrepancy is expected, as the constitutive model used in the aforementioned study was less accurate than the data-driven hyperelastic energy functions employed in the present work.

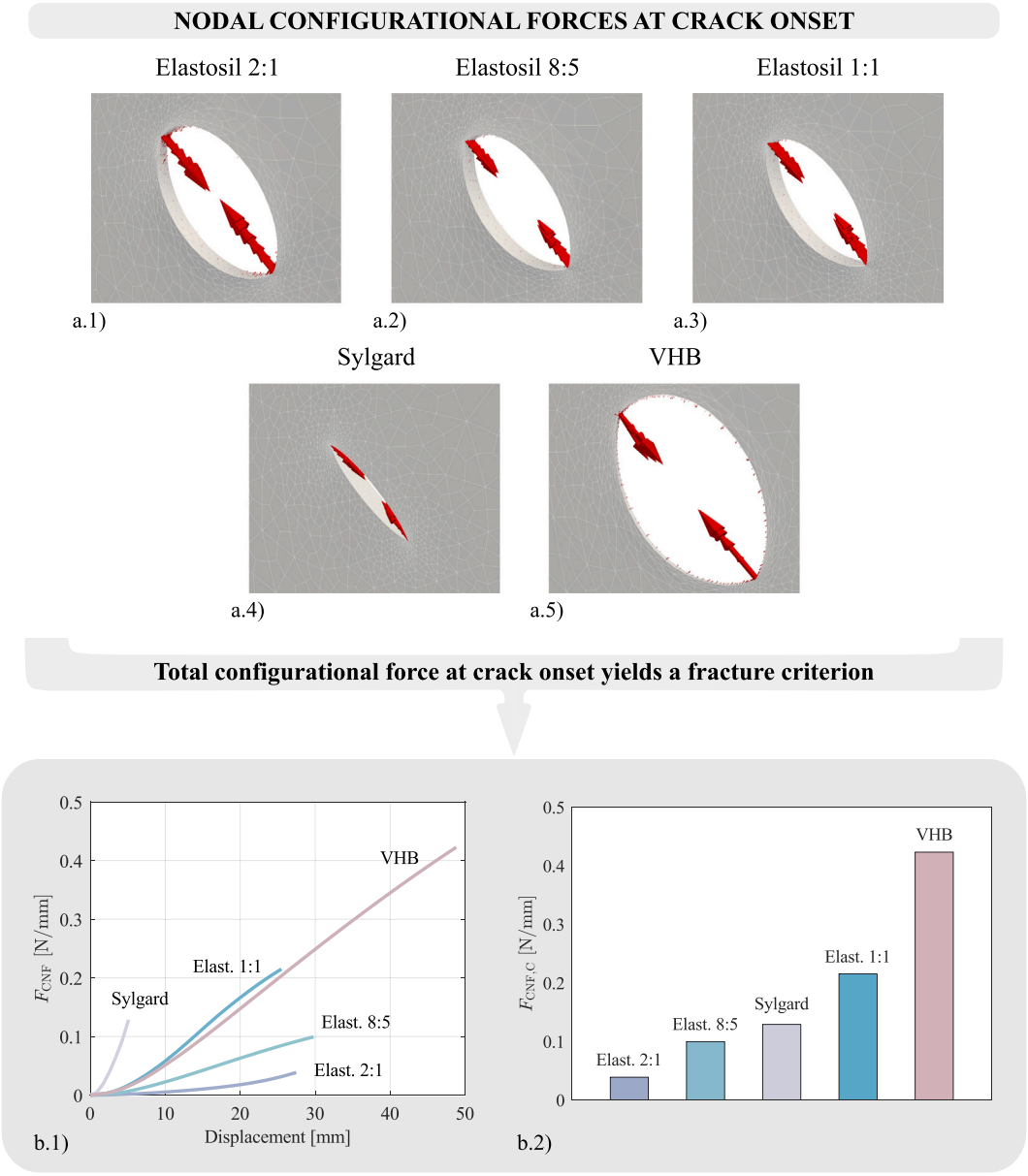

Fig. 12. Results for data-adaptive configurational forces *ante* crack onset and fracture criterion based on their critical values. (a) Nodal configurational forces at the crack tip and spurious configurational forces at the crack tip vicinity are depicted for Elastosil 2:1, Elastosil 8:5, Elastosil 1:1, Sylgard, and VHB at fracture onset. The loading stage selected in the virtual experiment (computation) is exactly the one corresponding to the displacement at crack onset (average values in Table A.2). Note that configurational forces are defined in the material configuration and here they are plotted in the spatial configuration to facilitate the visualization. Note also that the mesh used for the computation of configurational forces is identical to the non-symmetric mesh employed in the forward problem. Subsequently, (b.1) the nodal forces are added up to a crack tip total configurational force that is depicted as a function of the loading — displacement of the clamps — in the virtual experiment up to fracture onset. (b.2) The critical values of the configurational force for fracture initiation are depicted in a barplot, with the smallest value for Elastosil 2:1 and the largest value for VHB.

5. Discussion and outlook

5.1. Discussion

In the scope of this article, we have shown that the material characterization under multiaxial, quasi-static loading conditions plays a central role to accurately capture the constitutive behavior of soft elastomers. In turn, our data-adaptive framework

for hyperelastic energy functions proves versatility to capture biaxial experiments for different soft constitutive behaviors. This is paramount because accurately capturing the constitutive behavior of soft elastomers is key for a reliable application of the Configurational Force Method to soft solids.

Data-adaptive configurational forces for fracture require accurate constitutive models. Our framework combines reaction force data with full-field displacement measurements to calibrate hyperelastic energy functions. Displacement fields are extracted from equi-biaxial tests on five distinct soft elastomers — all with Young's modulus below $300\,\mathrm{kPa}$ — and featuring a centrally placed pre-cut that serves as strain concentrator and fracture initiator. The results reveal a spectrum of constitutive and fracture behaviors from brittle-like to highly deformable responses. Unlike pure VFM-based methods, which typically require full-field data across the entire surface, our FEMU-based optimization strategy remains unbiased even when the DIC data is incomplete. Notably, we find that the data-adaptive optimization of the hyperelastic energy functions based on biaxial test data primarily activates the first invariant strain energy function $\bar{\Psi}^{(I,\bar{I}_1)}$.

A fracture criterion is established based on a critical value of the crack tip configurational force $F_{\mathrm{CNF,C}}$. To capture the nonlinear, material-specific response of soft solids, we embed data-adaptive hyperelastic energy functions into the Configurational Force Method, enabling the computation of what we term *data-adaptive configurational forces for fracture*. A dedicated computational testbed replicates the biaxial experiments and leverages finite element solutions of the forward boundary value problem to evaluate the Eshelby stress tensor and associated nodal configurational forces. In the spirit of a fracture toughness material parameter, the crack tip configurational force at crack onset is a computationally efficient estimator of the J-integral. This approach captures the intricate constitutive behavior of soft materials under large geometrical nonlinearities, thereby offering a robust and efficient framework for fracture in highly deformable solids.

5.2. Outlook

Several experimental directions remain open for biaxial characterization of soft materials. Future studies could explore, among others, the effects of strain rate and deviations from equi-biaxial loading. In addition, promising opportunities lie in the multiaxial characterization of macroscale heterogeneous soft materials (Li et al., 2020; Moreno-Mateos and Steinmann, 2024b). In such systems, different fracture modes, such as sideways fracturing, could be studied together with micromechanical models that capture the intrinsic fracture mechanisms of soft polymers (see, e.g., Mulderrig et al., 2021).

A particularly promising extension of our framework for data-driven hyperelastic energy functions is its application to rate-dependent (viscoelastic) constitutive behavior. This may be achieved via a multiplicative decomposition of the deformation gradient into elastic and viscous parts, building upon a finite viscoelasticity model, such as the one proposed in Reese and Govindjee (1998).

Although our FEMU-based optimization method has demonstrated efficiency and robustness, a promising future direction lies in integrating of our data-adaptive hyperelastic energy functions with Physics-Informed Neural Networks. Recent work has shown that hyperelastic constitutive behavior can be represented using feed-forward neural networks (Hamel et al., 2023). This approach may eliminate the need for finite element forward simulations, making it an interesting benchmark for comparison.

Furthermore, the insights gained from our data-adaptive configurational force framework open new avenues for reverse engineering strategies that tailor the constitutive and fracture properties of soft materials through informed design and manufacturing parameters. In particular, neural network–based surrogate models hold promise for efficiently mapping observed mechanical behavior—such as hyperelasticity and fracture toughness—back to material formulation or processing variables. In this reversed workflow, learned parameters related to fracture serve as inputs, while outputs correspond to fabrication pathways related to, e.g., elastomer synthesis. In this context, our framework may provide a systematic and high-fidelity route to generate the curated datasets required to train such models, thereby enabling data-driven material design rooted in fracture mechanics.

Lastly, a point of interest is the extension to our framework to the *post* fracture onset regime. In this context, the use of configurational forces together with a fracture dissipation inequality may open new interesting routes to enable predictive modeling beyond crack initiation, paving the way toward a more comprehensive understanding of failure in highly deformable materials.

CRediT authorship contribution statement

Miguel Angel Moreno-Mateos: Writing – review & editing, Writing – original draft, Visualization, Validation, Methodology, Investigation, Formal analysis, Conceptualization. **Simon Wiesheier:** Writing – review & editing, Writing – original draft, Visualization, Validation, Methodology, Investigation, Formal analysis, Conceptualization. **Ali Esmaeili:** Writing – review & editing, Methodology. **Mokarram Hossain:** Writing – review & editing, Resources. **Paul Steinmann:** Writing – review & editing, Funding acquisition, Resources, Formal analysis.

Declaration of competing interest

The authors declare the following financial interests/personal relationships which may be considered as potential competing interests: Miguel Angel Moreno-Mateos reports financial support was provided by European Research Council. Simon Wiesheier reports financial support was provided by European Research Council. Mokarram Hossain reports was provided by Engineering and Physical Sciences Research Council. Paul Steinmann reports financial support was provided by European Research Council. If there are other authors, they declare that they have no known competing financial interests or personal relationships that could have appeared to influence the work reported in this paper.

Acknowledgments

Miguel Angel Moreno-Mateos, Simon Wiesheier, and Paul Steinmann acknowledge support from the European Research Council (ERC)[http://dx.doi.org/10.13039/501100000781] under the Horizon Europe program (Grant -No. 101052785, project: SoftFrac). Funded by the European Union. Views and opinions expressed are however those of the author(s) only and do not necessarily reflect those of the European Union or the European Research Council Executive Agency. Neither the European Union nor the granting authority can be held responsible for them. Mokarram Hossain acknowledges support from the Engineering and Physical Sciences Research Council (EPSRC), United Kingdom under the grant (EP/Z535710/1) and Royal Society (UK) under the International Exchange Grant (IEC/NSFC/211316).

Appendix A. Force–displacement results for each axis and experimental repetition

Individual repetitions, labeled 1 through 4, are shown explicitly to facilitate comparison with the raw data — force–displacement measurements and subsequent DIC fields — available on Zenodo. This also enables an assessment of the variability across experiments. Experimental variability is observed in both the initial slope of the force–displacement curves and the displacement at the onset of fracture for some experiments (see, e.g., Elastosil 2:1). This variability may stem from inconsistencies in the application of the initial notch as well as from small heterogeneities in the sample thickness introduced by the open-molding fabrication process.

Table A.2 contains the displacement values at crack onset for each material and for all experimental repetitions. Each repetition is labeled 1 through 4 to facilitate correlation with Fig. A.13, Table 1, and the raw dataset available on Zenodo.

Appendix B. Additional strain field results: experimental repetitions 2 – 4

See Figs. B.14–B.16.

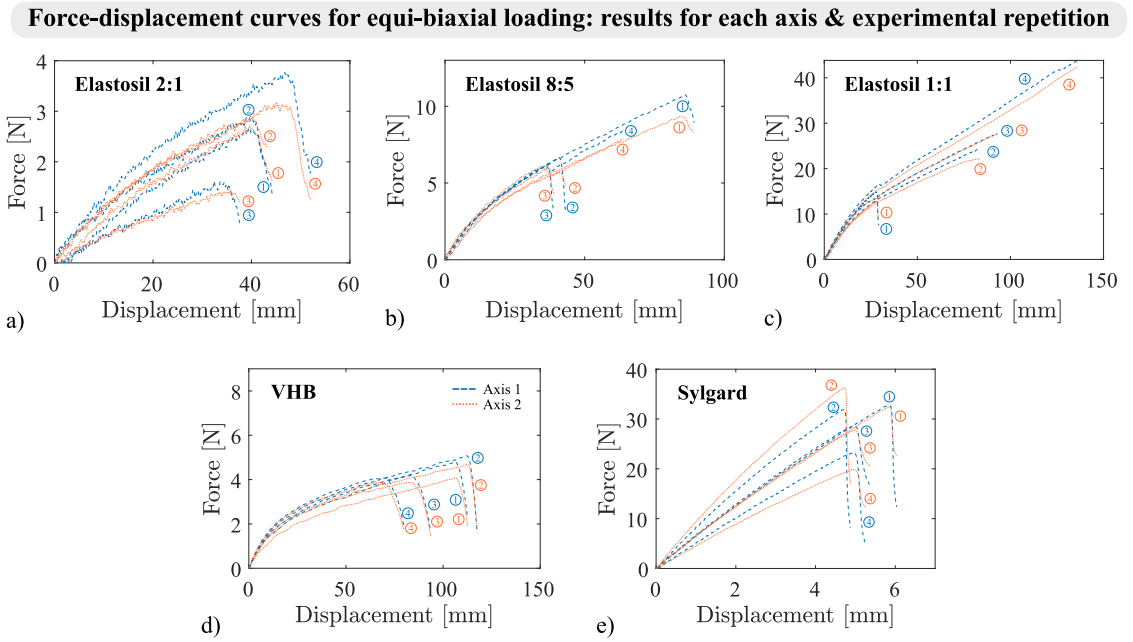

Fig. A.13. Experimental results for the biaxial experiments. The two independent axes move identically at a displacement rate of $0.85\,\mathrm{mm\,s^{-1}}$, which renders a strain rate of $0.01\,\mathrm{s^{-1}}$. (a–e) Force displacement results for equi-biaxial experiments and for each of the axes of the machine (blue and orange colored-lines), for Elastosil with mixing ratios of 2:1, 8:5, and 1:1, VHB, and Sylgard, respectively. The results for each experimental repetition are marked with ①, ②, ③, and ④ so that they can be easily identified in the Zenodo dataset. Four repetitions are performed for the same tests conditions.

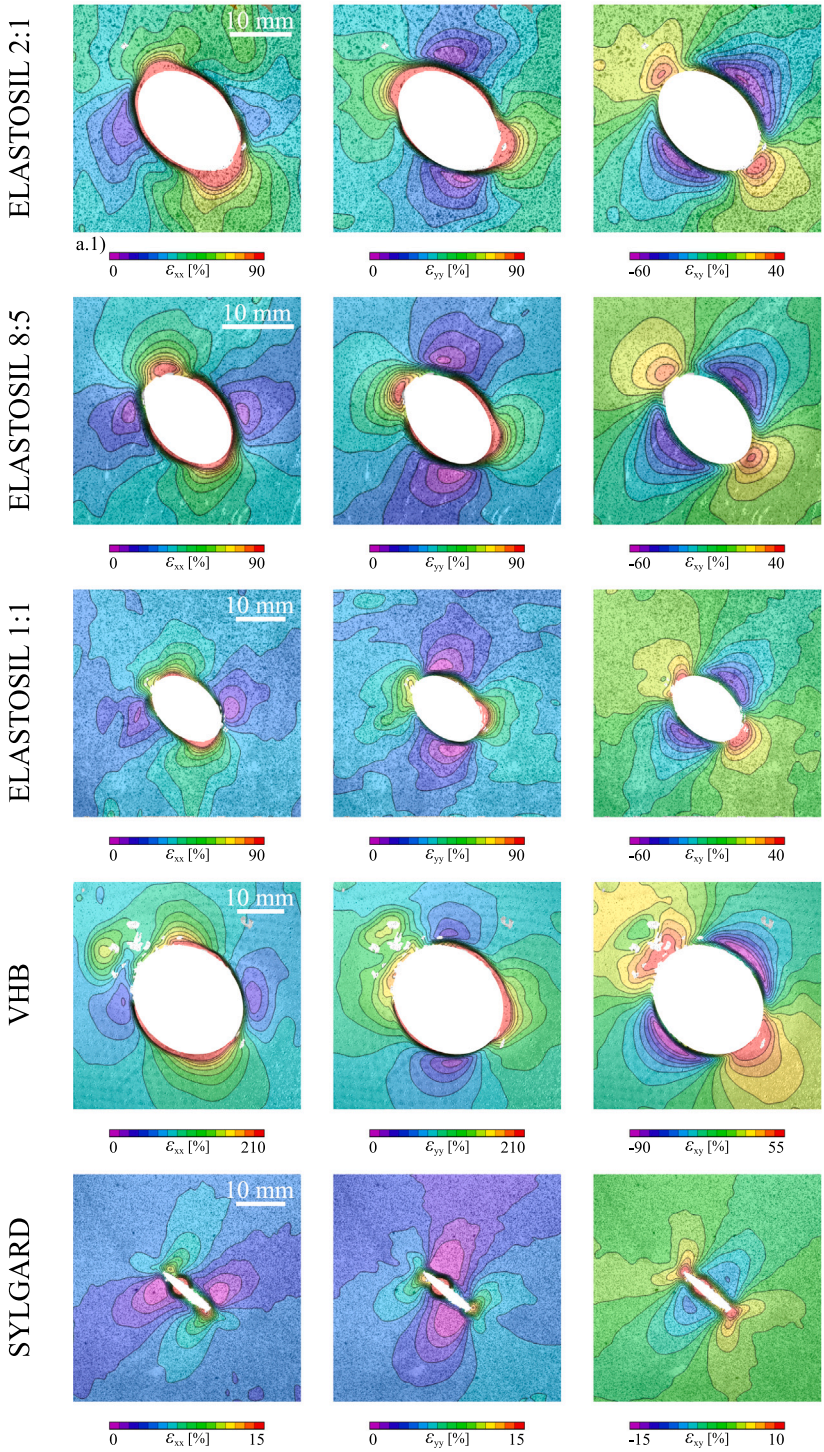

Fig. B.14. Strain fields at onset of crack growth for experimental repetition 2. The fields are engineering strain fields computed from the Lagrange strain tensor. The fields correspond to average engineering strains at crack onset of: 43.3 % for Elastosil 2:1, 36.6 % for Elastosil 8:5, 33.3 % for Elastosil 1:1, 76.7 % for VHB, and 6.1 % for Sylgard (see Fig. 2.a–e and Table 1). The fields correspond for Repetition ② (out of the four repetitions performed for the same type of sample and same test conditions). Note that x and y denote the horizontal and vertical directions, respectively. To improve the visual presentation of the results, custom white masks are applied to the regions corresponding to the interior of the deformed cracks.

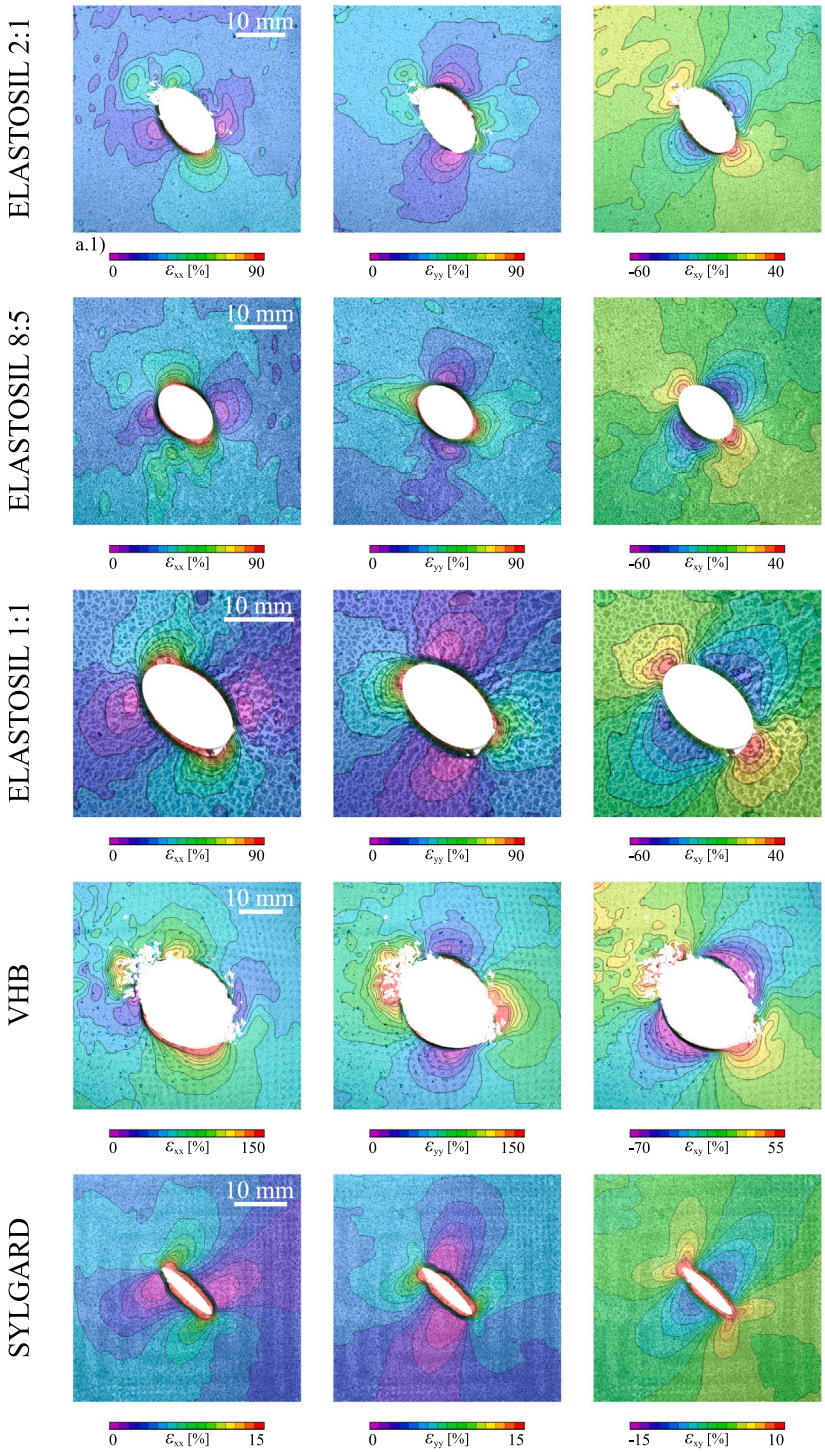

Fig. B.15. Strain fields at onset of crack growth for experimental repetition 3. The fields are engineering strain fields computed from the Lagrange strain tensor. The fields correspond to average engineering strains at crack onset of: 29.3 % for Elastosil 2:1, 33.3 % for Elastosil 8:5, 26.0 % for Elastosil 1:1, 68.0 % for VHB, and 6.2 % for Sylgard (see Fig. 2.a–e and Table 1). The fields correspond for Repetition ③ (out of the four repetitions performed for the same type of sample and same test conditions). Note that x and y denote the horizontal and vertical directions, respectively. To improve the visual presentation of the results, custom white masks are applied to the regions corresponding to the interior of the deformed cracks.

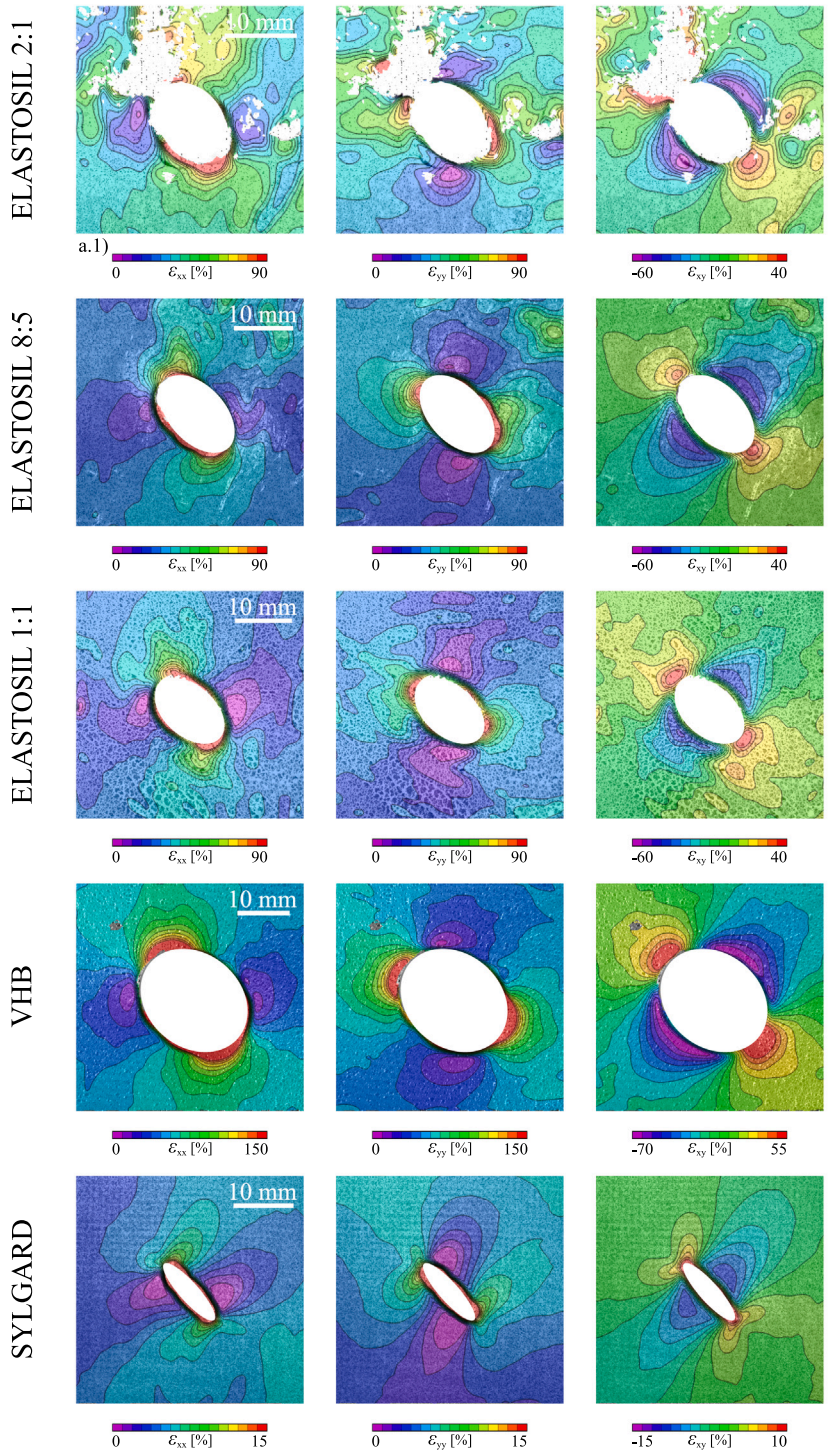

Fig. B.16. Strain fields at onset of crack growth for experimental repetition 4. The fields are engineering strain fields computed from the Lagrange strain tensor. The fields correspond to average engineering strains at crack onset of: 38.4 % for Elastosil 2:1, 27.6 % for Elastosil 8:5, 31.6 % for Elastosil 1:1, 35.1 % for VHB, and 6.7 % for Sylgard (see Fig. 2.a–e and Table 1). The fields correspond for Repetition ④ (out of the four repetitions performed for the same type of sample and same test conditions). Note that x and y denote the horizontal and vertical directions, respectively. To improve the visual presentation of the results, custom white masks are applied to the regions corresponding to the interior of the deformed cracks.

Table A.2
Experimental results for the displacement at the onset of crack extension. The displacement at crack onset corresponds to the instant when initial crack growth take place—and not when full rupture occurs, which is reported in Fig. 3. The results are identified from the images for the four experimental repetitions (denoted as "Rep."). The mean values and standard deviation for each material are included.

	Rep.	Elastosil 2:1	Elastosil 8:5	Elastosil 1:1	VHB	Sylgard
Displacement at crack onset [mm]	1	15.6	36.3	27.5	42.5	6.3
	2	36.8	31.1	28.3	65.2	5.2
	3	24.9	28.3	22.1	57.8	5.3
	4	32.6	23.5	26.9	29.8	5.7
		27.5 ± 8.08	29.8 ± 4.63	26.2 ± 2.42	48.8 ± 13.7	5.6 ± 0.4

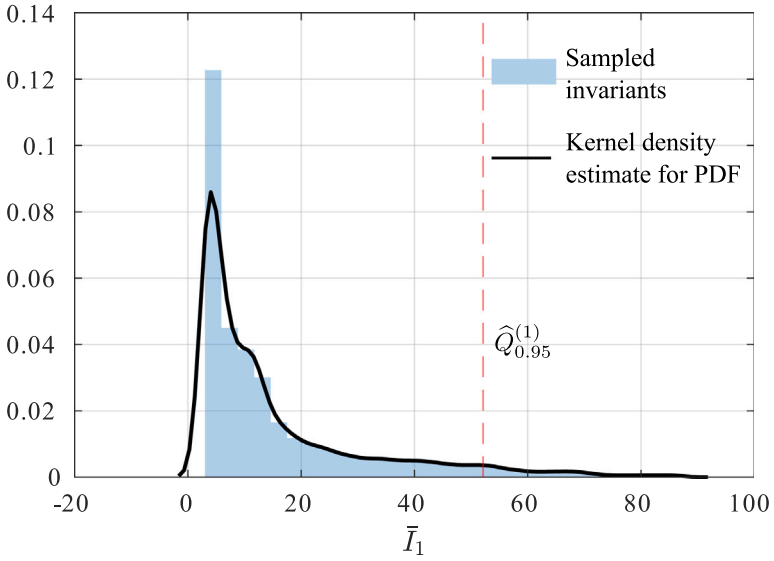

Fig. C.17. Kernel Density Estimation (KDE) employed to obtain a differentiable representation of the probability density function (PDF) for the sampled invariants $\bar{I}_1, \bar{I}_2$.

Appendix C. Kernel density estimation

At each optimization iteration, the sampled invariants $(\bar{I}_1, \bar{I}_2)$ at the quadrature points of the FE mesh are transferred into a histogram. Fig. C.17 illustrates mocked $\bar{I}_1$ values obtained from a forward solve. While a histogram plot groups these samples into discrete bins and yields a discrete probability density function (PDF), the resulting representation is not continuously differentiable. This is problematic because the gradient-based optimizer *fmincon* requires the objective function to be continuously differentiable with respect to all optimization variables. For example, computing the 95-quantile $\widehat{Q}^{(1)}_{0.95}$ directly from the histogram would violate this differentiability assumption.

To address this, we apply kernel density estimation (KDE), which produces a smooth and continuously differentiable approximation of the PDF. In this approach, each sampled value contributes a smooth kernel function, and the overall PDF is obtained by summing these kernels.

The required 95-quantile $\widehat{Q}^{(1)}_{0.95}$, as used in Eq. (10), is extracted by evaluating the inverse cumulative density function (iCDF) of the KDE

$$\widehat{Q}^{(1)}_{0.95} =: F^{-1}_{\bar{I}_1}(0.95). \tag{C.1}$$

Using a Gaussian kernel, the PDF and the corresponding CDF are given by

$$\text{PDF:} \quad f_{\bar{I}_1}(x) = \frac{1}{nh}\sum_{i=1}^{n} K\left(\frac{x - x_i}{h}\right) \quad K(x) = \frac{1}{\sqrt{2\pi}}\exp\left(-\frac{1}{2}x^2\right), \tag{C.2}$$

$$\text{CDF:} \quad F_{\bar{I}_1}(x) = \frac{1}{n}\sum_{i=1}^{n} G\left(\frac{x - x_i}{h}\right) \quad G(x) = 0.5\left[1 + \text{erf}\left(\frac{x}{\sqrt{2}}\right)\right], \tag{C.3}$$

with n the number of samples.

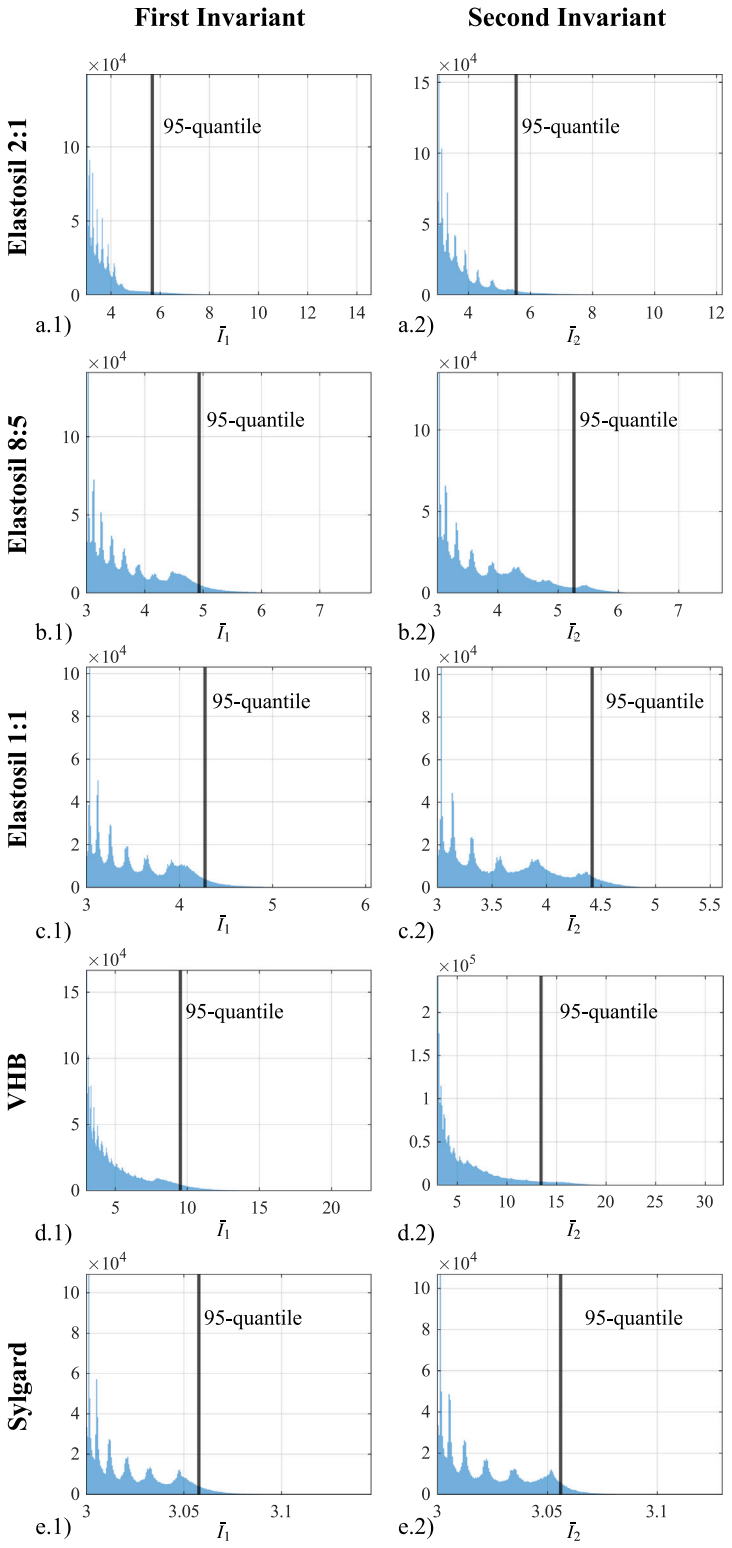

Fig. D.8. Sampled invariants predicted by the FE forward simulation using the identified data-adaptive hyperelastic strain energy functions. The vertical line marks the 95th-percentile of the invariants.

The bandwidth h is defined as

$$h = \left[\frac{4}{3n}\right]^{1/5} \sigma, \tag{C.4}$$

where σ is the standard deviation of the samples. This choice is optimal for normally distributed data and provides a sufficiently accurate approximation of the sampled invariant distribution for our purposes (Atkinson et al., 0000). We aggregated all samples at the quadrature points in each load step of the forward solve. A more efficient sampling strategy (e.g., sampling invariants only at specific geometric locations and load steps) is left for future work. The above steps are identically applied to the second invariant $\bar{I}_2$.

Appendix D. Sampled invariants in the FE forward boundary value problem

The histograms in Fig. D.8 show the distributions of the invariants $\bar{I}_1$ and $\bar{I}_2$ as predicted by the forward simulations for each material's identified strain energy function. The histograms are constructed from the invariant values evaluated at all quadrature points of the finite element mesh, aggregated across all simulation load steps. The vertical lines mark the 95th percentile of each distribution.

The overall range and shape of the $\bar{I}_1$ and $\bar{I}_2$ distributions are similar for the three Elastosil variants and for Sylgard. In contrast, the VHB material exhibits a noticeably wider spread between the two invariants, as reflected in the respective 95th-percentile values, which are 9.52 for $\bar{I}_1$ and 13.44 for $\bar{I}_2$. This behavior can be qualitatively understood by considering the simplified case of equibiaxial tension, where the invariants take the form (Steinmann et al., 2012)

$$\bar{I}_1 = \lambda^{-4} + 2\lambda^2, \tag{D.1}$$

$$\bar{I}_2 = 2\lambda^{-2} + 2\lambda^4. \tag{D.2}$$

These expressions illustrate that the difference between $\bar{I}_1$ and $\bar{I}_2$ increases with the applied deformation λ. However, in our biaxial experiments the applied deformation (less than 100 % engineering strain) is not large enough to induce a pronounced separation between the two invariants. Among all materials, Sylgard exhibits the narrowest range of sampled invariants, staying below 3.1. The visible peaks in the histograms correspond to the invariant values sampled at discrete simulation load steps.

A key quantity extracted from the histograms is the 95th-percentile value, which we approximate using kernel density estimation (cf. Appendix C). This estimate helps align the interpolation domain of the strain energy function with the range of actually sampled invariants. Comparing the rightmost interpolation point in Figs. 7–11a with the 95th-percentile values in Fig. D.8 indicates good agreement. This demonstrates that the discretized invariant space of our data-driven hyperelastic energy functions is neither too narrow nor unnecessarily wide relative to the actual sampled invariants triggered by the data.

Appendix E. Supplementary data

Supplementary material related to this article can be found online at https://doi.org/10.1016/j.jmps.2025.106339.

Data availability

The experimental datasets are available in https://doi.org/10.5281/zenodo.15187640.

References

Abdusalamov, R., Hillgärtner, M., Itskov, M., 2023. Automatic generation of interpretable hyperelastic material models by symbolic regression. Int. J. Numer. Methods Eng. 124, 2093–2104.
Ahmad, D., Sahu, S.K., Patra, K., 2019. Fracture toughness, hysteresis and stretchability of dielectric elastomers under equibiaxial and biaxial loading. Polym. Test. 79, 106038.
Arif, Z.U., Khalid, M.Y., Tariq, A., Hossain, M., Umer, R., 2024. 3D printing of stimuli-responsive hydrogel materials: Literature review and emerging applications. Giant 17, 100209.
Arndt, D., et al., 2021. The deal.II finite element library: Design, features, and insights. Comput. Math. Appl. 81, 407–422.
Arndt, D., et al., 2022. The deal.II Library, Version 9.4.
Arunachala, P.K., et al., 2024. A multiscale anisotropic polymer network model coupled with phase field fracture. Int. J. Numer. Methods Eng. 125, e7488.
Atkinson, A.C., Copas, J.B., Pierce, D.A., Schervish, M.J., Titterington, D.M., 0000. oxford statistical Science Series. Oxford Statistical Science Series.
Bahmani, B., Sun, W., 2024. Physics-constrained symbolic model discovery for polyconvex incompressible hyperelastic materials. Int. J. Numer. Methods Eng. 125, e7473.
Ball, J.M., 1976. Convexity conditions and existence theorems in nonlinear elasticity. Arch. Ration. Mech. Anal. 63, 337–403.
Behnke, R., Berger, T., Kaliske, M., 2018. Numerical modeling of time- and temperature-dependent strain-induced crystallization in rubber. Int. J. Solids Struct. 141–142, 15–34.
Belytschko, T., Lu, Y.Y., Gu, L., Tabbara, M., 1995. Element-free galerkin methods for static and dynamic fracture. Int. J. Solids Struct. 32, 2547–2570.
d. Boor, C., 1978. A Practical Guide To Splines. Springer Verlag.
Budiansky, B., Rice, J.R., 1973. Conservation laws and energy-release rates. J. Appl. Mech. 40, 201–203.
Cherepanov, G.P., 1967. Crack propagation in continuous media. J. Appl. Math. Mech. 31, 503–512.
Dal, H., Denli, F.A., Ačan, A.K., Kaliske, M., 2023. Data-driven hyperelasticity, part i: A canonical isotropic formulation for rubberlike materials. J. Mech. Phys. Solids 179, 105381.
Dammaß, F., Kalina, K.A., Kaestner, M., 2024a. Neural networks Meet Phase-Field: A Hybrid Fracture Model.

Dammaß, F., Kalina, K.A., Kästner, M., 2025. When invariants matter: The role of i1 and i2 in neural network models of incompressible hyperelasticity. Mech. Mater. 210, 105443.
Dammaß, F., Schab, D., Rohm, H., Kästner, M., 2024b. Rate- and temperature-dependent ductile-to-brittle fracture transition: Experimental investigation and phase-field analysis for toffee. Eng. Fract. Mech. 297, 109878.
Denzer, R., Barth, F.J., Steinmann, P., 2003. Studies in elastic fracture mechanics based on the material force method. Int. J. Numer. Methods Eng. 58, 1817–1835.
Denzer, R., Menzel, A., 2014. Configurational forces for quasi-incompressible large strain electro-viscoelasticity–application to fracture mechanics. Eur. J. Mech. - A/Solids 48, 3–15.
Dugdale, D., 1960. Yielding of steel sheets containing slits. J. Mech. Phys. Solids 8, 100–104.
Ellmer, N., Ortigosa, R., Martínez-Frutos, J., Gil, A.J., 2024. Gradient enhanced gaussian process regression for constitutive modelling in finite strain hyperelasticity. Comput. Methods Appl. Mech. Eng. 418, 116547.
Erdogan, F., Sih, G.C., 1963. On the crack extension in plates under plane loading and transverse shear. J. Basic Eng. 85, 519–525.
Eshelby, J.D., 1951. The force on an elastic singularity. Philos. Trans. R. Soc. Lond. 244.
Eshelby, J.D., 1975. The elastic energy-momentum tensor. J. Elast. 5, 321–335.
Eshelby, J.D., 1999. Energy relations and the energy-momentum tensor in continuum mechanics. In: Fundamental Contributions To the Continuum Theory of Evolving Phase Interfaces in Solids. pp. 82–119.
Esmaeili, A., George, D., Masters, I., Hossain, M., 2023. Biaxial experimental characterizations of soft polymers: A review. Polym. Test. 128, 108246.
Flaschel, M. others, 2023. Automated discovery of interpretable hyperelastic material models for human brain tissue with EUCLID. J. Mech. Phys. Solids 180, 105404.
Francfort, G.A., Marigo, J.J., 1998. Revisiting brittle fracture as an energy minimization problem. J. Mech. Phys. Solids 46, 1319–1342.
Frankel, A.L., Jones, R.E., Swiler, L.P., 2019. Tensor basis Gaussian Process Models of Hyperelastic Materials. ArXiv. abs/1912.10872.
Frankl, S.M., Pletz, M., Schuecker, C., 2022. Improved concept for iterative crack propagation using configurational forces for targeted angle correction. Eng. Fract. Mech. 266, 108403.
Fuhg, J. N. others, 2025. A Review on Data-Driven Constitutive Laws for Solids. Arch. Comput. Methods Eng. 32, 1841–1883.
Griffith, A.A., 1921. The phenomena of rupture and flow in solids. philosophical transactions of the royal society a: Mathematical. Phys. Eng. Sci. 221, 163–198.
Gross, D., Kolling, S., Mueller, R., Schmidt, I., 2003. Configurational forces and their application in solid mechanics. Eur. J. Mech. - A/Solids 22, 669–692.
Guo, Y., Li, Q., 2017. Material configurational forces applied to mixed mode crack propagation. Theor. Appl. Fract. Mech. 89, 147–157.
Gurtin, M.E., Podio-Guidugli, P., 1996. Configurational forces and the basic laws for crack propagation. J. Mech. Phys. Solids 44, 905–927.
Hamel, C.M., Long, K.N., Kramer, S.L.B., 2023. Calibrating constitutive models with full-field data via physics informed neural networks. Strain 59, e12431.
Holthusen, H., Lamm, L., Brepols, T., Reese, S., Kuhl, E., 2024. Theory and implementation of inelastic constitutive artificial neural networks. Comput. Methods Appl. Mech. Eng. 428, 117063.
Hu, X., Li, S., 2025. A stress-intensity-factor-driven phase field modeling of mixed mode fracture. Comput. Methods Appl. Mech. Eng. 443, 118058.
Hui, C.Y., Jagota, A., Bennison, S.J., Londono, J.D., 2003. Crack blunting and the strength of soft elastic solids. proceedings of the royal society of London. Series a: Mathematical. Phys. Eng. Sci. 459, 1489–1516.
Hussain, M., Pu, S., Underwood, J., 1974. Strain energy release rate for a crack under combined mode i and mode ii. In: National Symposium on Fracture Mechanics. pp. 2–2–27.
Irwin, G., 1957. Analysis of stresses and strains near the end of a crack traversing a plate. J. Appl. Mech. 24, 361–364.
James, A.G., Green, A., Simpson, G.M., 1975. Strain energy functions of rubber. i. characterization of gum vulcanizates. J. Appl. Polym. Sci. 19, 2033–2058.
Javili, A., Ekiz, E., McBride, A.T., Steinmann, P., 2021. Continuum-kinematics-inspired peridynamics: Thermo-mechanical problems. Contin. Mech. Thermodyn. 33, 2039–2063.
Jirásek, M., 1998. Nonlocal models for damage and fracture: Comparison of approaches. Int. J. Solids Struct. 35, 4133–4145.
Joshi, A. others, 2022. Bayesian-EUCLID: Discovering hyperelastic material laws with uncertainties. Comput. Methods Appl. Mech. Eng. 398, 115225.
Kaliske, M., Netzker, C., Näser, B., 2009. Evaluation of crack-driving forces at finite viscoelasticity: Theory and experiment. IUTAM Bookseries 17, 193–202.
Kawabata, S., Matsuda, M., Tei, K., Kawai, H., 1981. Experimental survey of the strain energy density function of isoprene rubber vulcanizate. Macromol. 14, 154–162.
Khiêm, V.N., Mai, T.-T., Urayama, K., Gong, J.P., Itskov, M., 2019. A multiaxial theory of double network hydrogels. Macromol. 52, 5937–5947.
Kienzler, R., Herrmann, G., 1997. On the properties of the eshelby tensor. Acta Mech. 125, 73–91.
Kienzler, R., Herrmann, G., Haslach, H., 2002. Mechanics in material space: With applications to defect and fracture mechanics. Appl. Mech. Rev. 55, B23–B24.
Kirchdoerfer, T., Ortiz, M., 2016. Data-driven computational mechanics. Comput. Methods Appl. Mech. Eng. 304, 81–101.
Klein, D.K., et al., 2025. Neural networks meet hyperelasticity: A monotonic approach. ArXiv:2501.02670. [cs].
Kolednik, O., Tiwari, A., Posch, C., Kegl, M., 2022. Configurational force based analysis of creep crack growth. Int. J. Fract. 236, 175–199.
Kumar, A., Bourdin, B., Francfort, G.A., Lopez-Pamies, O., 2020. Revisiting nucleation in the phase-field approach to brittle fracture. J. Mech. Phys. Solids 142, 104027.
Li, F., Shih, C., Needleman, A., 1985. A comparison of methods for calculating energy release rates. Eng. Fract. Mech. 21, 405–421.
Li, C., Yang, H., Suo, Z., Tang, J., 2020. Fatigue-resistant elastomers. J. Mech. Phys. Solids 134, 103751.
Linden, L. others, 2023. Neural networks meet hyperelasticity: A guide to enforcing physics. J. Mech. Phys. Solids 179, 105363.
Linka, K. others, 2021. Constitutive artificial neural networks: A fast and general approach to predictive data-driven constitutive modeling by deep learning. J. Comput. Phys. 429, 110010.
Linka, K., Kuhl, E., 2023. A new family of Constitutive Artificial Neural Networks towards automated model discovery. Comput. Methods Appl. Mech. Eng. 403, 115731.
Liu, R., Hou, J., Li, Q., 2020. Material configurational forces applied to mixed-mode fatigue crack propagation and life prediction in elastic-plastic material. Int. J. Fatigue 134, 105467.
Lo, Y.-S., Hughes, T.J., Landis, C.M., 2022. Phase-field fracture modeling for large structures. J. Mech. Phys. Solids 105118.
Long, R., Hui, C.-Y., 2015. Crack tip fields in soft elastic solids subjected to large quasi-static deformation—a review. Extrem. Mech. Lett. 4, 131–155.
Long, R., Krishnan, V.R., Hui, C.Y., 2011. Finite strain analysis of crack tip fields in incompressible hyperelastic solids loaded in plane stress. J. Mech. Phys. Solids 59, 672–695.
Lu, Y., Qi, Y., Tenardi, M., Long, R., 2021. Mixed-mode fracture in a soft elastomer. Extrem. Mech. Lett. 48, 101380.
Miehe, C., Welschinger, F., Hofacker, M., 2010. Thermodynamically consistent phase-field models of fracture: Variational principles and multi-field fe implementations. Int. J. Numer. Methods Eng. 83, 1273–1311.
Moës, N., Dolbow, J., Belytschko, T., 1999. A finite element method for crack growth without remeshing. Int. J. Numer. Methods Eng..
Mooney, M., 1940. A theory of large elastic deformation. J. Appl. Phys. 11, 582–592, Publisher: American Institute of Physics.
Moran, B., Shih, C.F., 1987. Crack tip and associated domain integrals from momentum and energy balance. Eng. Fract. Mech. 27, 615–642.
Moreno-Mateos, M.A., Hossain, M., Steinmann, P., Garcia-Gonzalez, D., 2022. Hybrid magnetorheological elastomers enable versatile soft actuators. Npj Comput. Mater. 8, 162.
Moreno-Mateos, M.A., Hossain, M., Steinmann, P., Garcia-Gonzalez, D., 2023. Hard magnetics in ultra-soft magnetorheological elastomers enhance fracture toughness and delay crack propagation. J. Mech. Phys. Solids 173, 105232.

Moreno-Mateos, M.A., Mehnert, M., Steinmann, P., 2024. Electro-mechanical actuation modulates fracture performance of soft dielectric elastomers. Int. J. Eng. Sci. 195, 104008.
Moreno-Mateos, M.A., Steinmann, P., 2024a. Configurational force method enables fracture assessment in soft materials. J. Mech. Phys. Solids 186, 105602.
Moreno-Mateos, M.A., Steinmann, P., 2024b. Crosslinking degree variations enable programming and controlling soft fracture via sideways cracking. Npj Comput. Mater. 10, 282.
Moučka, R., Sedlačík, M., Osička, J., Pata, V., 2021. Mechanical properties of bulk sylgard 184 and its extension with silicone oil. Sci. Rep. 11, 19090.
Mulderrig, J., Buche, M., Grasinger, M., 2025. Polydisperse polymer networks with irregular topologies. Arxiv.
Mulderrig, J., Li, B., Bouklas, N., 2021. Affine and non-affine microsphere models for chain scission in polydisperse elastomer networks. Mech. Mater. 160.
Näser, B., Kaliske, M., Müller, R., 2007. Material forces for inelastic models at large strains: Application to fracture mechanics. Comput. Mech. 40, 1005–1013.
Nguyen, T.D., Govindjee, S., Klein, P.A., Gao, H., 2005. A material force method for inelastic fracture mechanics. J. Mech. Phys. Solids 53, 91–121.
Ortigosa, R., et al., 2025. A generalized theory for physics-augmented neural networks in finite strain thermo-electro-mechanics. Comput. Methods Appl. Mech. Eng. 437, 117741.
Özenç, K., Kaliske, M., Lin, G., Bhashyam, G., 2014. Evaluation of energy contributions in elasto-plastic fracture: A review of the configurational force approach. Eng. Fract. Mech. 115, 137–153.
Pancheri, F.Q., Dorfmann, L., 2014. Strain-controlled biaxial tension of natural rubber: New experimental data. Rubber Chem. Technol. 87, 120–138.
Peerlings, R., de Borst, R., Brekelmans, W., Geers, M., 1998. Gradient-enhanced damage modelling of concrete fracture. Mech. Cohesive-Frictional Mater. 3, 323–342.
Piegl, L., Tiller, W., 1996. The NURBS Book, second ed. Springer-Verlag, New York, NY, USA.
Pierron, F., Grédiac, M., 2012. The Virtual Fields Method: Extracting Constitutive Mechanical Parameters from Full-Field Deformation Measurements. Springer, New York, NY.
Podio-Guidugli, P., 2002. Configurational forces: are they needed? Mech. Res. Commun. 29, 513–519.
Qi, Y., Zou, Z., Xiao, J., Long, R., 2019. Mapping the nonlinear crack tip deformation field in soft elastomer with a particle tracking method. J. Mech. Phys. Solids 125, 326–346.
Reese, S., Govindjee, S., 1998. A theory of finite viscoelasticity and numerical aspects. Int. J. Solids Struct. 35, 3455–3482.
Rice, J.R., 1968. A path independent integral and the approximate analysis of strain concentration by notches and cracks. J. Appl. Mech. 35, 379.
Ricker, A., Wriggers, P., 2023. Systematic Fitting and Comparison of Hyperelastic Continuum Models for Elastomers. Arch. Comput. Methods Eng. 30, 2257–2288.
Römer, U., et al., 2024. Reduced and all-at-Once Approaches for Model Calibration and Discovery in Computational Solid Mechanics. ArXiv:2404.16980. [cs].
Schmidt, B., Fraternali, F., Ortiz, M., 2009. Eigenfracture: An eigendeformation approach to variational fracture. 7, pp. 1237–1266.
Schmitz, K., Ricoeur, A., 2023. Theoretical and computational aspects of configurational forces in three-dimensional crack problems. Int. J. Solids Struct. 282, 112456.
Schreyer, H.L., 1990. Analytical solutions for nonlinear strain-gradient softening and localization. J. Appl. Mech. 57, 522–528.
Schütte, H., 2009. Curved crack propagation based on configurational forces. Comput. Mater. Sci. 46, 642–646.
Serrao, P.H., Kozinov, S., 2025a. Configurational forces for defect evolution in flexoelectricity. Eng. Fract. Mech. 110903.
Serrao, P.H., Kozinov, S., 2025b. Evaluation of configurational/material forces in strain gradient elasticity theory. Mech. Mater. 203, 105240.
Shih, C.F., Moran, B., Nakamura, T., 1986. Energy release rate along a three-dimensional crack front in a thermally stressed body. Int. J. Fract. 30, 79–102.
Shivakumar, K.N., Raju, I.S., 1992. An equivalent domain integral method for three-dimensional mixed-mode fracture problems. Eng. Fract. Mech. 42, 935–959.
Sih, G.C., 1974. Strain-energy-density factor applied to mixed mode crack problems. Int. J. Fract. 10, 305–321.
Silling, S.A., 2000. Reformulation of elasticity theory for discontinuities and long-range forces. J. Mech. Phys. Solids 48, 175–209.
Song, J.H., Wang, H., Belytschko, T., 2008. A comparative study on finite element methods for dynamic fracture. Comput. Mech. 42, 239–250.
Steinmann, P., 2000. Application of material forces to hyperelastostatic fracture mechanics. i. continuum mechanical setting. Int. J. Solids Struct. 37, 7371–7391.
Steinmann, P., 2008. On boundary potential energies in deformational and configurational mechanics. J. Mech. Phys. Solids 56, 772–800.
Steinmann, P., 2022. Spatial and Material Forces in Nonlinear Continuum Mechanics, vol. 272, Springer International Publishing.
Steinmann, P., Ackermann, D., Barth, F., 2001. Application of material forces to hyperelastostatic fracture mechanics. ii. computational setting. Int. J. Solids Struct. 38, 5509–5526.
Steinmann, P., Hossain, M., Possart, G., 2012. Hyperelastic models for rubber-like materials: consistent tangent operators and suitability for Treloar's data. Arch. Appl. Mech. 82, 1183–1217.
Steinmann, P., Scherer, M., Denzer, R., 2009. Secret and joy of configurational mechanics: From foundations in continuum mechanics to applications in computational mechanics. ZAMM - J. Appl. Math. Mech. / Z. Angew. Math. Und Mech. 89, 614–630.
Steinmann, P., d. Villiers, A., McBride, A., Javili, A., 2023. Configurational peridynamics. Mech. Mater. 185, 104751.
Storm, J., Kaliske, M., 2023. The origin of the energy split in phase-field fracture and eigenfracture. PAMM 23, e202300295.
Strifors, H.C., 1974. A generalized force measure of conditions at crack tips. Int. J. Solids Struct. 10, 1389–1404.
Stumpf, H., Makowski, J., Hackl, K., 2010. Configurational forces and couples in fracture mechanics accounting for microstructures and dissipation. Int. J. Solids Struct. 47, 2380–2389.
Sutton, M.A., Orteu, J.J., Schreier, H., 2009. Image Correlation for Shape, Motion and Deformation Measurements: Basic Concepts, Theory and Applications. Springer Science & Business Media.
Thakolkaran, P., et al., 2022. NN-EUCLID: Deep-learning hyperelasticity without stress data. J. Mech. Phys. Solids 169, 105076.
Tikenoğulları, O.Z., Açan, A.K., Kuhl, E., Dal, H., 2023. Data-driven hyperelasticity, part ii: A canonical framework for anisotropic soft biological tissues. J. Mech. Phys. Solids 181, 105453.
Treloar, L.R.G., 1944. Stress-strain data for vulcanised rubber under various types of deformation. Trans. Faraday Soc. 40, 59–70.
Wells, A., 1961. Unstable crack propagation in metals: Cleavage and fast fracture. In: Proceedings of the Crack Propagation Symposium, vol. 1, p. 84, Crack Tip Opening Displacement (CTOD).
Wiesheier, S., Mergheim, J., Steinmann, P., 2023. Discrete data-adaptive approximation of hyperelastic energy functions. Comput. Methods Appl. Mech. Eng. 416, 116366.
Wiesheier, S., Moreno-Mateos, M.A., Steinmann, P., 2024. Versatile data-adaptive hyperelastic energy functions for soft materials. Comput. Methods Appl. Mech. Eng. 430, 117208.
Yan, S., Schlüter, A., Müller, R., 2023. Configurational forces in a phase field model for fatigue. PAMM 22, e202200034.
Yeoh, O., 1990. Characterization of elastic properties of carbon-black-filled rubber vulcanizates. Rubber Chem. Technol. 63, 792–805.
Zhao, X., 2017. Designing toughness and strength for soft materials. Proc. Natl. Acad. Sci. 114, 8138–8140.
Zhou, R., Coombs, W.M., Xu, Y., Zhang, P., Wang, L.G., 2022. A configurational force-based material point method for crack propagation modelling in 2d. Theor. Appl. Fract. Mech. 117, 103186.